N 69 38650
NASA CR 106046

NATIONAL AERONAUTICS AND SPACE ADMINISTRATION

Technical Report 32-1391

The Far Encounter Planet Sensor

D. G. Carpenter

CASE FILE
COPY

JET PROPULSION LABORATORY
CALIFORNIA INSTITUTE OF TECHNOLOGY
PASADENA, CALIFORNIA

September 1, 1969

NATIONAL AERONAUTICS AND SPACE ADMINISTRATION

Technical Report 32-1391

The Far Encounter Planet Sensor

D. G. Carpenter

JET PROPULSION LABORATORY
CALIFORNIA INSTITUTE OF TECHNOLOGY
PASADENA, CALIFORNIA

September 1, 1969

Prepared Under Contract No. NAS 7-100
National Aeronautics and Space Administration

Preface

The work described in this report was performed by the Guidance and Control Division of the Jet Propulsion Laboratory.

Since the completion of this report, the two *Mariner* spacecraft have successfully encountered Mars and transmitted a large number of excellent photographs and a great volume of valuable scientific data back to earth. The far encounter planet sensor performed as predicted on both spacecraft. The *Mariner VI* FEPS was operated from encounter minus 51 hours to encounter minus 76 hours; the *Mariner VII* FEPS performed from encounter minus 76 hours to encounter minus 1 hour and 41 minutes. Thus with the completion of the *Mariner VII* encounter, the FEPS project was brought to a totally successful conclusion.

Contents

Tables

Figures

Contents (contd)

Figures (contd)

Abstract

The far encounter planet sensor (FEPS) is an electro-optical device that is mounted on the *Mariner* Mars 1969 spacecraft. The planet sensor provides two-axis pointing signals to the scan control subsystem for directing the spacecraft scan platform toward the center of the illuminated portion of Mars during the far encounter phase of the spacecraft mission. The sensor operational requirements, a general operational description, and a detailed description of each major part of the sensor are discussed. Also discussed are the fabrication methods and problems, and a complete analysis of functional test results.

The Far Encounter Planet Sensor

I. Introduction

The far encounter planet sensor (FEPS), an electro-optical device, will be used during the far encounter phase of the *Mariner* Mars 1969 spacecraft mission. The FEPS provides two-axis pointing signals to the scan control subsystem to direct the spacecraft scan platform toward the center of the illuminated portion of Mars. The FEPS error signals are proportional to the displacement between the center of the illuminated portion of Mars and the FEPS optical axis. The FEPS also produces an electrical signal that will indicate when Mars is within the FEPS field-of-view. The FEPS is aligned to the optical axis of the high resolution television camera mounted on the scan platform.

Light from Mars entering the objective lens of the FEPS is focused on detectors in two different locations by means of a beam-splitting mirror. Each of the two silicon photovoltaic detectors is a dual unit, consisting of two half-cells. The half-cells are sequentially connected to a single amplifier by a multiplex (time-shared) modulator so that a simple radiometric balance is obtained in each control axis when the FEPS is properly pointed at the radiometric centroid of Mars. The error signal transfer function is 10 V/deg over a linear range of ± 1 deg. A saturated output is maintained from the ± 1 deg to the edge of the FEPS field-of-view at ± 5 deg.

Automatic gain control (AGC) is provided by means of pulse width modulation of the samples from the detector half-cells. Automatic gain control is required because the planet subtense changes from 0.285 deg to 1.40 deg during the far encounter phase as the spacecraft approaches Mars. The change in the FEPS illuminance may be as much as 24.2 to 1. The AGC signal is derived from the sum of the voltage output of the four half-cells.

A planet-in-field-of-view (PIFOV) signal is derived from the AGC signal to act as a threshold indication that the FEPS is functioning and that the error signals are available for controlling the scan platform servo system. The FEPS has no moving parts. Both 2400-Hz square-wave power and 15-Vdc power are used. The error signals are conventional phase-reversing dc signals, and the planet-in-field-of-view signal is a level change from zero to approximately 4.6 V.

II. General Operation

The FEPS (Figs. 1 and 2) consists of a lens and beam splitter, two bisected silicon detectors, and signal processing electronics. The lens collects the radiant energy within a circular field-of-view of ±5 deg. The spectral sensitivity of the FEPS is determined by the detectors and is nominally 0.4 to 1.1 μ. The beam splitter, which is half-silvered in a polka dot pattern, distributes this energy equally between the two silicon detectors. The image on these detectors is defocused to provide an essentially linear transfer function over a range of ±1 deg. The detectors are oriented for sensitivity in orthogonal axes. Figure 3 presents the FEPS alignment axis and field-of-view designations.

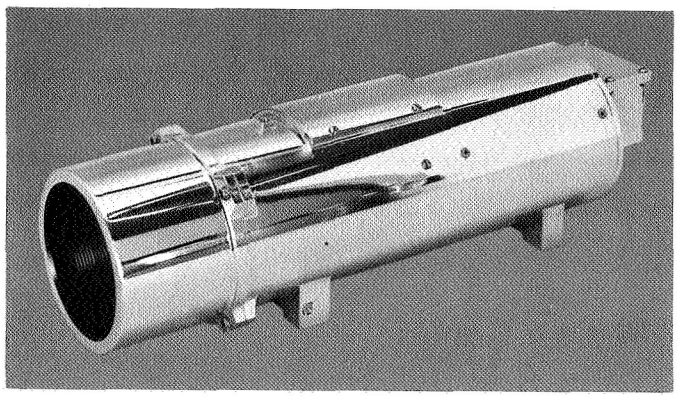

Fig. 1. Far encounter planet sensor

The electronics sequentially samples the voltages generated by each half-cell of the detectors. A synchronous detector develops a dc voltage which is an analog of planet intensity. This voltage is used to modify the sampling periods to normalize for changes in planet intensity, thus providing a type of automatic gain control. The signals are then decommutated and fed to integrating output amplifiers. The decommutation provides a signal to the output amplifiers that is the algebraic difference between the signals generated on opposite half-cells. The time constant of the integrating dc output amplifiers smooths the samples to provide a clean dc output signal. The polarity and magnitude of this voltage is an analog of the sign and magnitude of the angular tracking error.

Table 1 presents a summary of the FEPS nominal operating parameters. All parameters in the original design were met or exceeded in the final configuration.

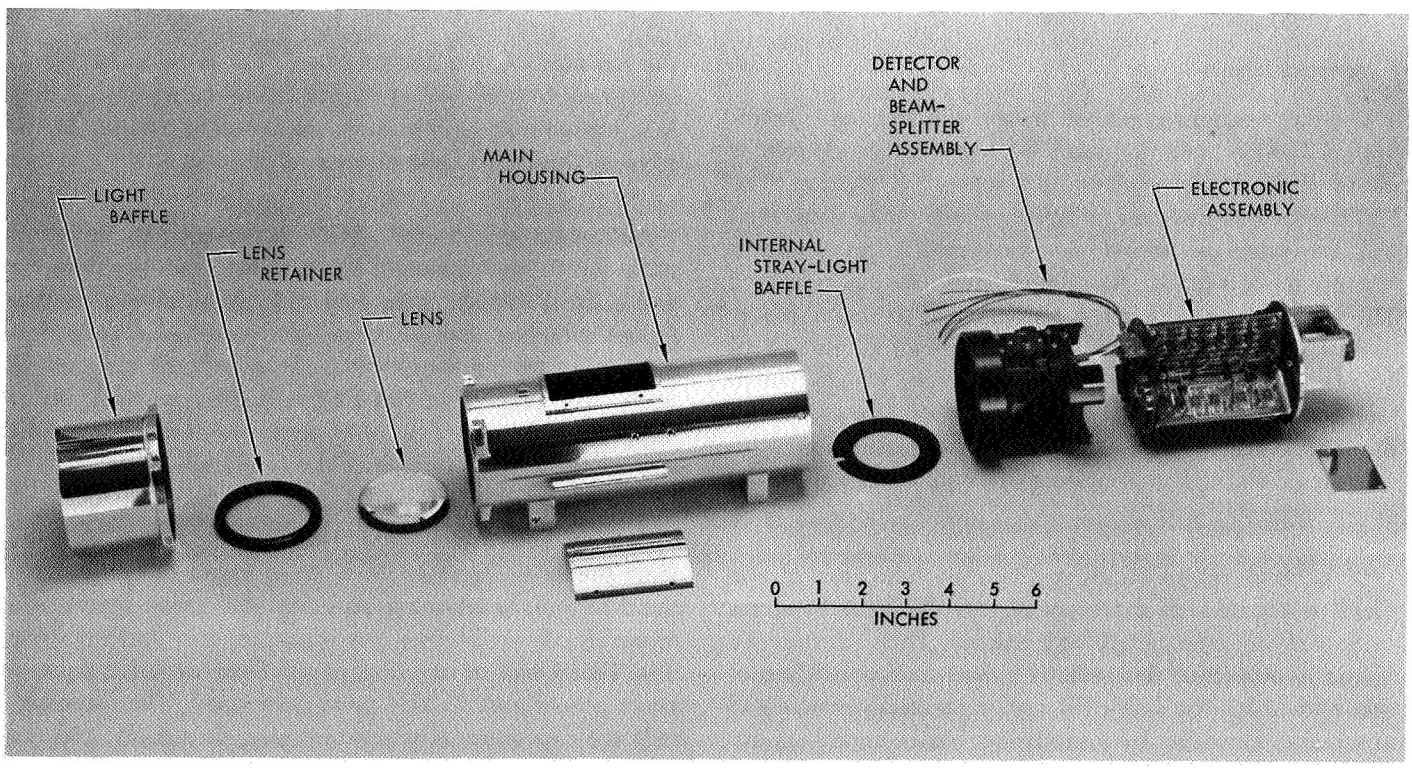

Fig. 2. Far encounter planet sensor (exploded view)

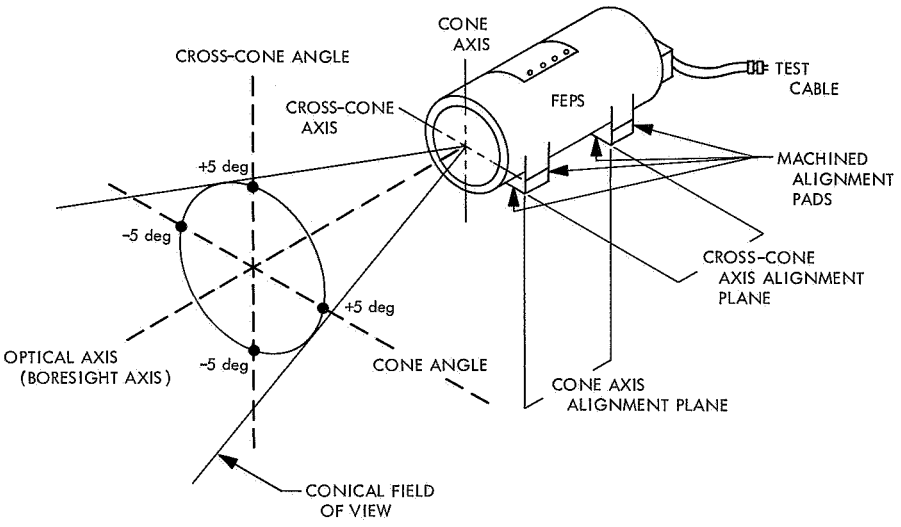

Fig. 3. Field-of-view designations

Table 1. Nominal parameters of the FEPS

Parameter	Nominal values	Parameter	Nominal values
Error signals		Mounting alignment (around line of sight)	0.4 deg
Signal type	dc analog		
Two-axis error output		Planet-in-field-of-view signal (PIFOV)	
Total range (saturated)	±5 deg	Signal type	dc digital
Linear range	±1 deg	Signal magnitudes	
Linearity	0.3 V/deg	PIFOV	4.6 ±0.5 V
Scale factor	10 V/deg ±30%	No PIFOV	−0.5 ±0.5 V
Automatic gain control range	25:1	Output impedance	5 kΩ
Frequency response (−3 dB)	10 Hz	Time delay (turn off)	1 s
Output impedance	1 kΩ	Miscellaneous parameters	
Threshold and resolution	0.01 deg		
Accuracy	0.2 deg	Power consumption	0.75 W
Channel separation	43 dB (Corresponds to an orthogonality of 0.4 deg)	Weight	2.3 lb
		Volume	75 $in.^3$

III. Detailed Design

A. Mechanical

The mechanical configuration of the FEPS consists of four major component parts as shown in Fig. 2. The housing is a cylindrical section approximately 3 in. in diameter and 8 in. long. The housing includes integral mounting feet with steel inserts located in such a way that mounting is accomplished by bolting through the mounting surface into the sensor.

The heart of the FEPS is the beam-splitter housing and assembly shown in Fig. 4. This assembly houses both silicon detector assemblies and the polka dot beam splitter. The beam-splitter assembly slides into the main housing and is positioned with respect to the lens (focused) by means of a threaded rod connected to the main housing. This rod also acts as a positive axial locking device for the beam-splitter assembly by means of the jam nut on the shaft end. Built into the beam-splitter housing are the translational adjustment devices for both

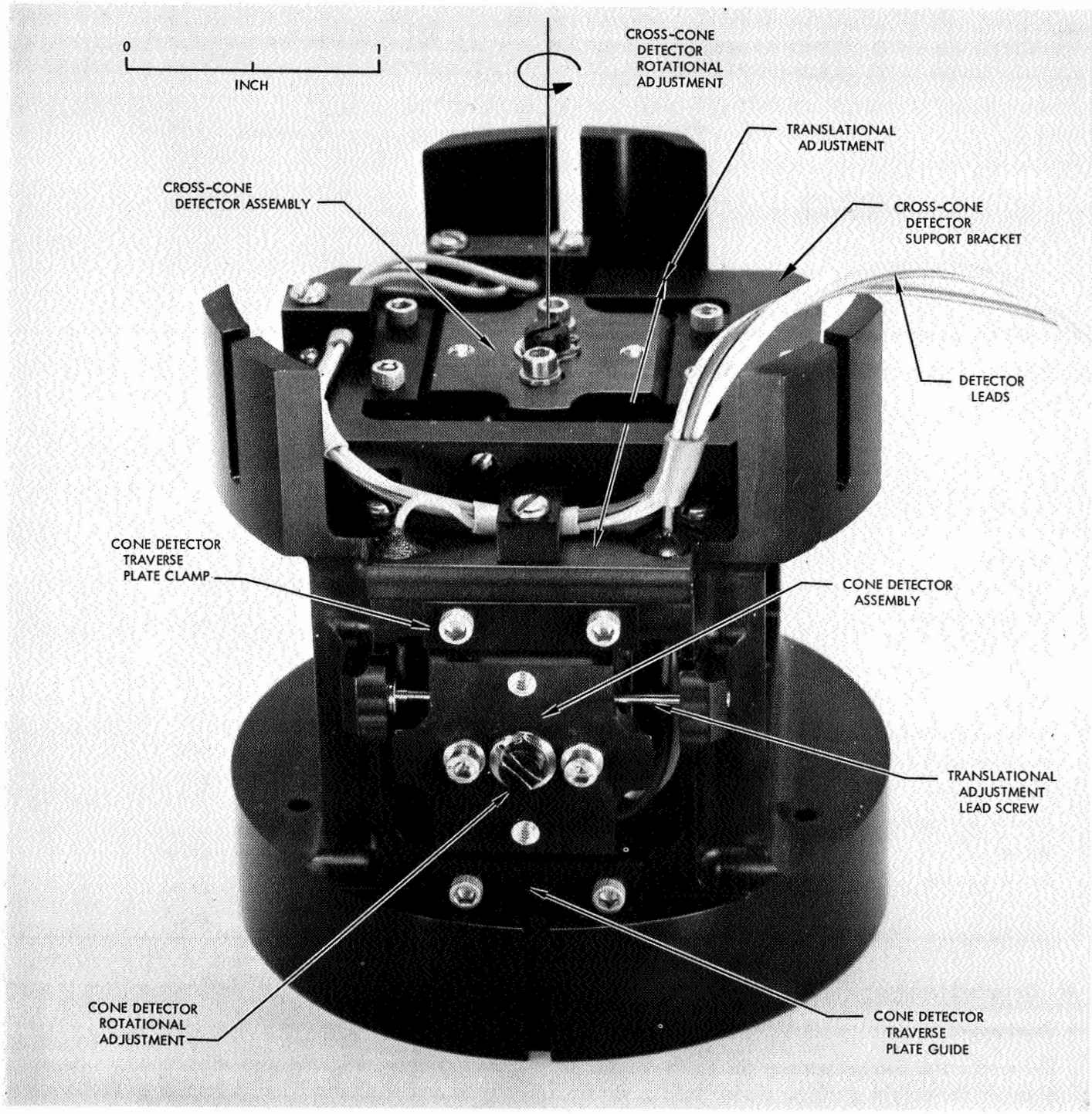

Fig. 4. Beam-splitter housing and detector assembly

detector assemblies, providing for translational adjustment of the detectors with respect to the optical axis of the sensor. This adjustment allows the cell bisecting line to fall exactly on the optical axis, thereby greatly reducing null errors and increasing overall pointing accuracy.

The support bracket of the cross-cone detector shown in Fig. 3 is shimmed off the beam-splitter housing by a stack of 0.010 shims. This allows the position of the two detectors, relative to one another, to be varied by a change of the total shim thickness. The two detectors are then focused together with respect to the lens by moving the beam-splitter housing. Thus the focus can be critically adjusted so that the defocused image of the planet on each detector is identical and, therefore, the final output curves for both axes have identical characteristics. The other requirement of adjustment is the rotational adjustment of each cell around the cone and cross-cone axes of the sensor. Rotation ensures that the bisecting line of the cone detectors lies parallel to the mounting plane and the bisecting line of the cross-cone detectors lies perpendicular to the mounting plane. Thus the requirements for orthogonality and channel separation imposed on the sensor output are met.

The electronics assembly is a unique design consisting of a Y-web-shaped structure with seven small printed circuit boards mounted on each side of the three webs (Fig. 5). Although there are approximately 130 components on the boards, the design allows complete accessibility both for mounting components and intercabling, and for rework if necessary.

The last major mechanical component part is the light baffle shown in Fig. 2. Because the stray-light environment in which the FEPS must operate on the spacecraft is very favorable for an optical sensor, a complex optical stray-light baffle was not required. In the present design the baffle acts merely as a light shade.

B. Optical

The optical system of the FEPS, comprising the lens beam splitter, the detectors, and the processing electronics, is shown in a simplified schematic (Fig. 6). The

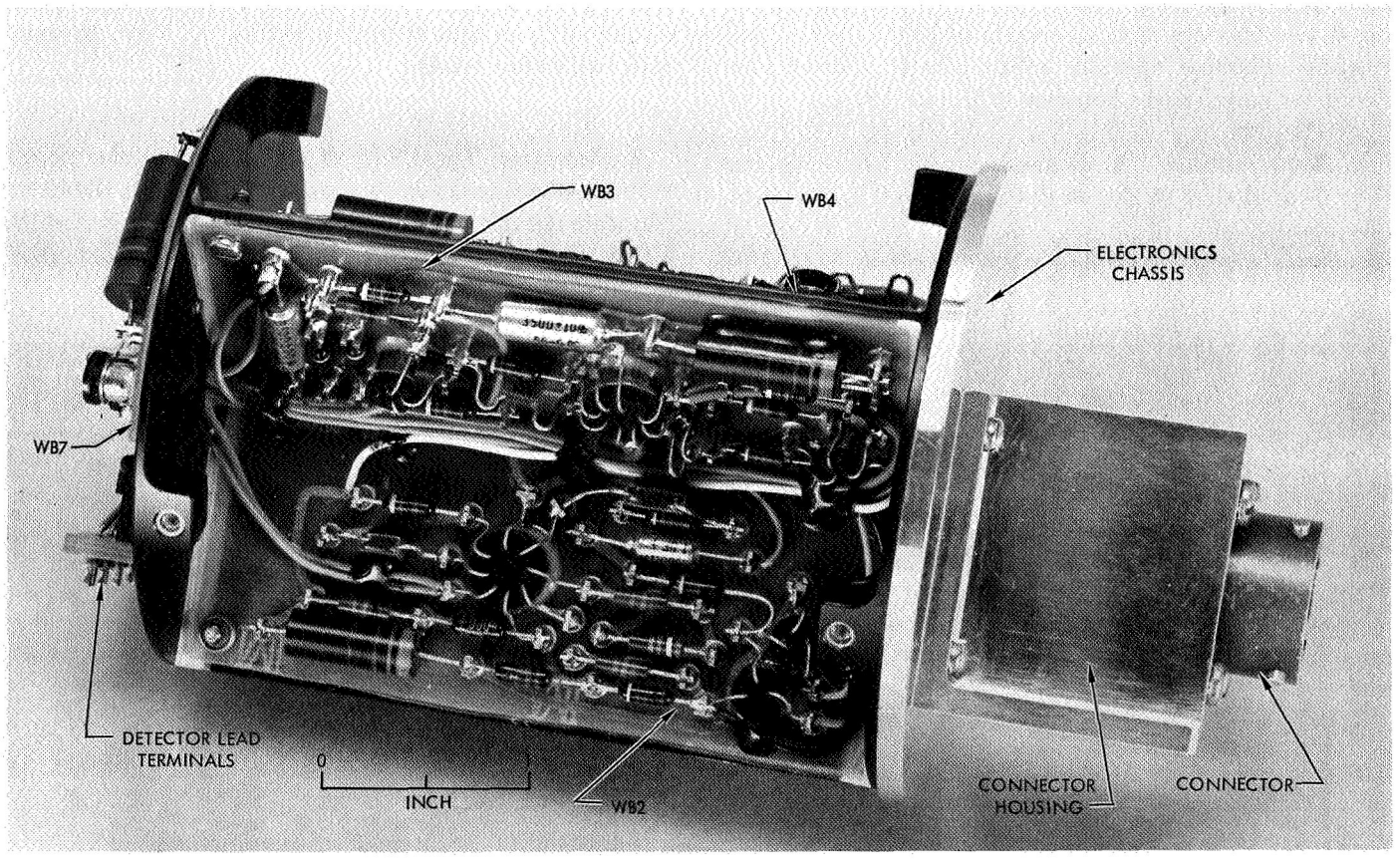

Fig. 5. FEPS electronics assembly

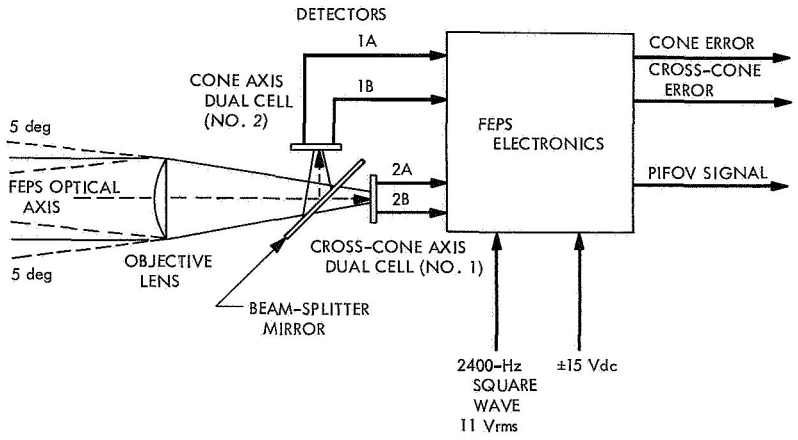

Fig. 6. FEPS simplified schematic

following is a description of the major components of the optical system.

1. Lens. The objective lens is a plano-convex with an effective focal length (EFL) of 3.5 in. and an effective diameter of 2.0 in. The lens is fabricated from fused quartz (Homosil[1]) and is coated with an anti-reflection coating of magnesium fluoride (MgF_2). The MgF_2 coating is vacuum-deposited to a depth of 1360 Å, which will provide minimum specular reflectance at normal incidence for wavelengths between 0.70 and 0.80 μ.

2. Beam splitter. A high-efficiency beam splitter (Fig. 7) angled at 45 deg to the optical axis lies immediately behind the objective lens. This beam splitter, unique in its construction, consists of a 0.062-in. fused-quartz plate with a surface of vacuum-deposited aluminum polka dots that act as individual mirrors. The dots, each 0.049 in. in diameter, are deposited in a rectangular grid pattern. The ratio of reflecting area to transmitting area is adjusted to evenly divide the radiant energy between the two detectors. Both surfaces of the beam splitter are coated with an anti-reflective coating of MgF_2 to minimize reflective losses.

3. Detectors. The FEPS detectors are circular photovoltaic silicon cells approximately 0.6 in. in diameter. The detector diameter and lens EFL combine to define the FEPS field-of-view, which is a 10-deg circular cone.

[1]Engelhard Industries, Amersil Quartz Div., Hillside, N. J. 07205.

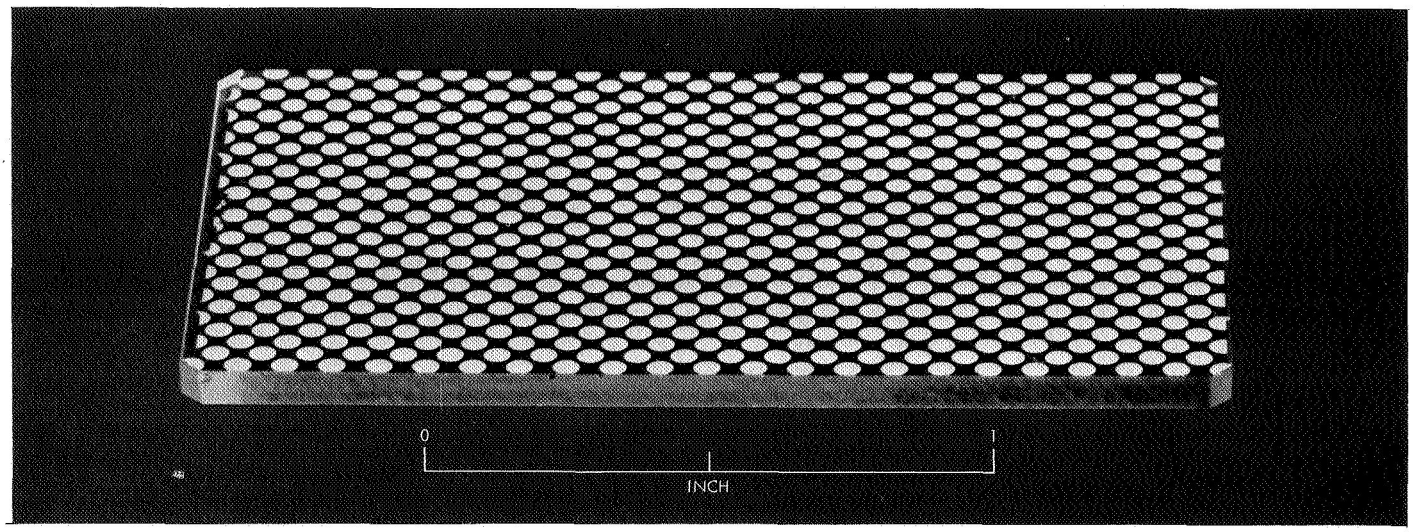

Fig. 7. High-efficiency beam splitter

The dual feature of the detector was obtained by producing a mesa-etched border and dividing line that delineates the active cell areas and provides a common anode. The cathode leads are soldered to an electroless nickel solderable area that is deposited around the periphery of the detector. As Fig. 8 shows, the entire dual detector is sweat-soldered to a kovar base in which terminals are provided for connection to the two cathode leads. A third terminal on the base provides electrical access to the base (anode) of the detector.

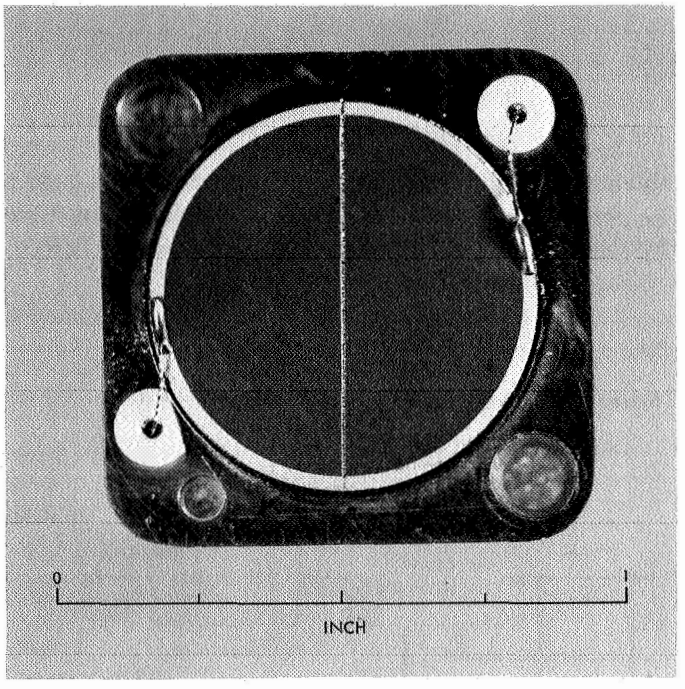

Fig. 8. Silicon detector

The silicon detector was fabricated from n on p 10-ohm-cm material because this material has the highest radiation resistance and gives good performance at low levels of light. The diffusion depth (obtained from a 90-min diffusion time) was chosen for maximum voltage output rather than for the maximum power output required for solar cells.

Silicon is a good choice of detector for Mars since the spectral sensitivity of silicon and the spectral intensity of Mars light are similar (Fig. 9).[2]

C. Electronic

The following text describes in detail the electronic operation and circuitry of the FEPS. For tracing the

[2]The silicon detectors used in the FEPS are a custom design manufactured by Textron Electronics, Inc., Heliotek Div., Sylmar, Calif. 91342. The controlling specification is presented as Appendix B.

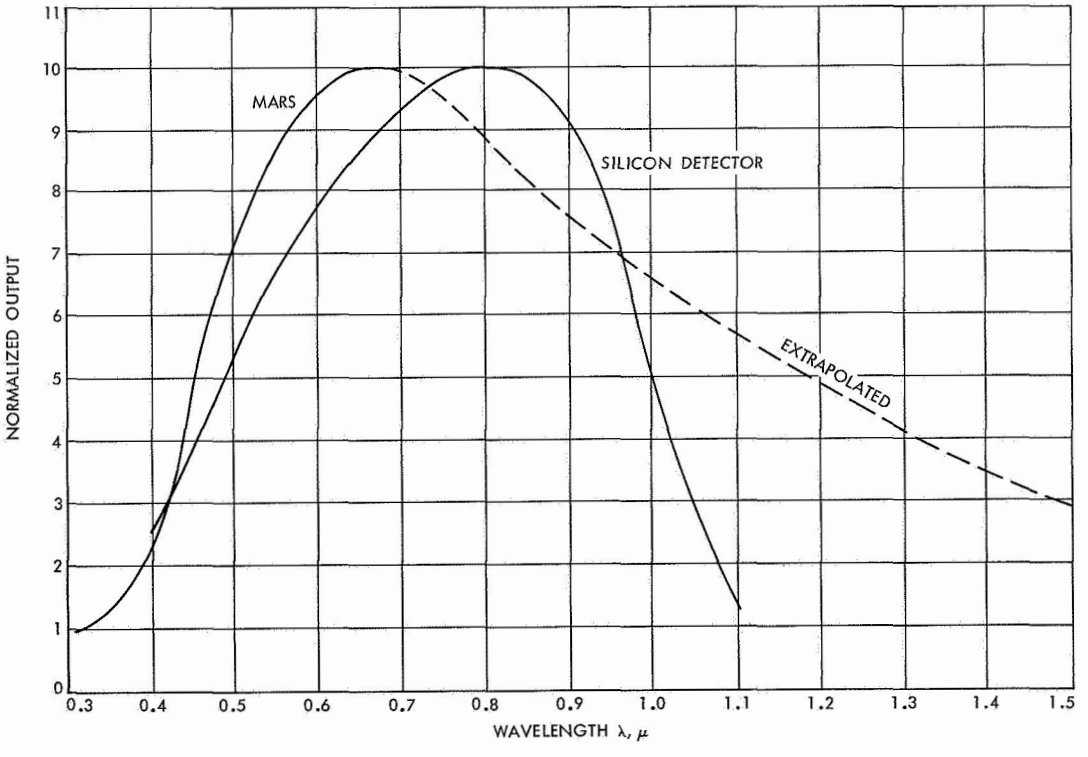

Fig. 9. Spectral energy distribution of Mars at full phase and silicon detector spectral response

detector signals through the system, the FEPS block diagram (Fig. 10) and the FEPS schematic diagram (Fig. 11) should be referred to. The system wave forms are shown in Fig. 12.

1. Detectors. When a planet is in the field-of-view of the FEPS, a defocused image of that planet will be formed on each detector. This image, at zero tracking error, will be symmetrically divided between the two half-cells. As the image moves across the detector the voltage output of one half-cell increases while the voltage output of the other half-cell decreases. It is this difference in voltage that is used to produce an output error function proportional to the angular displacement of the planet from the optical axis of the FEPS. The half-cell voltages developed under typical tracking conditions will be between 1.0 and 50.0 mV.

2. Detector loads. Each half-cell is connected to a parallel RC network located on WB7.[3] The resistances of these networks can vary between 33 kΩ and 51 kΩ, depending on the selection made at final calibration. The *responsivity* of each of the cell halves is normalized by the selection of this resistor. Responsivity is defined here as *cell output voltage for unit irradiance.*

The capacitor is 0.1 μF in each case. This capacitor integrates the cell output and permits the cell voltage to be periodically sampled with the minimum loading effect by the sampling circuit. A typical wave form of detector voltage is illustrated in *e* of Fig. 12.

[3]The designation *WB7* refers to *wiring board 7*, or *printed circuit-board 7*. The FEPS schematic (Fig. 11) is divided into seven blocks, each one with a WB-number.

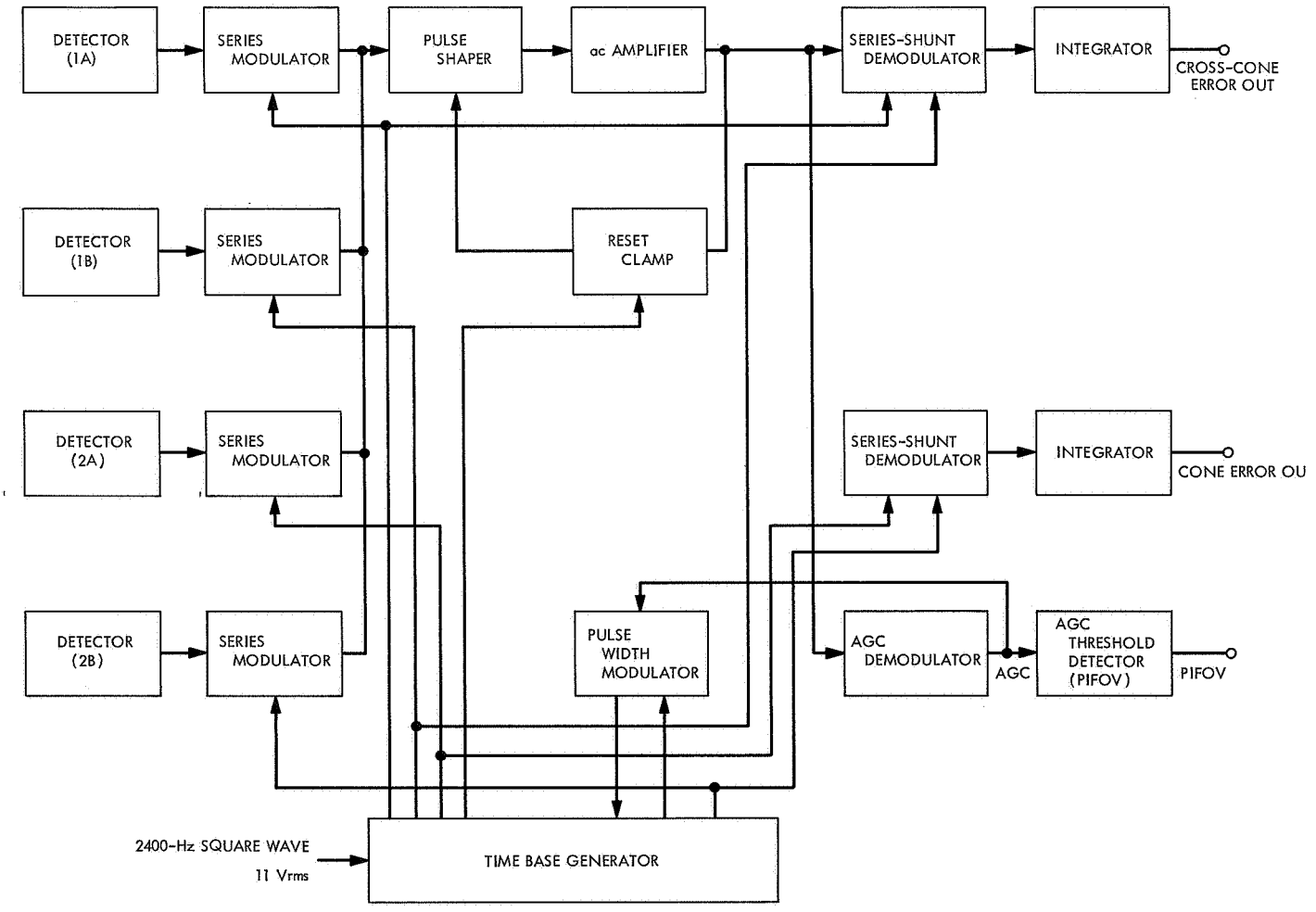

Fig. 10. Block diagram of the FEPS electronics

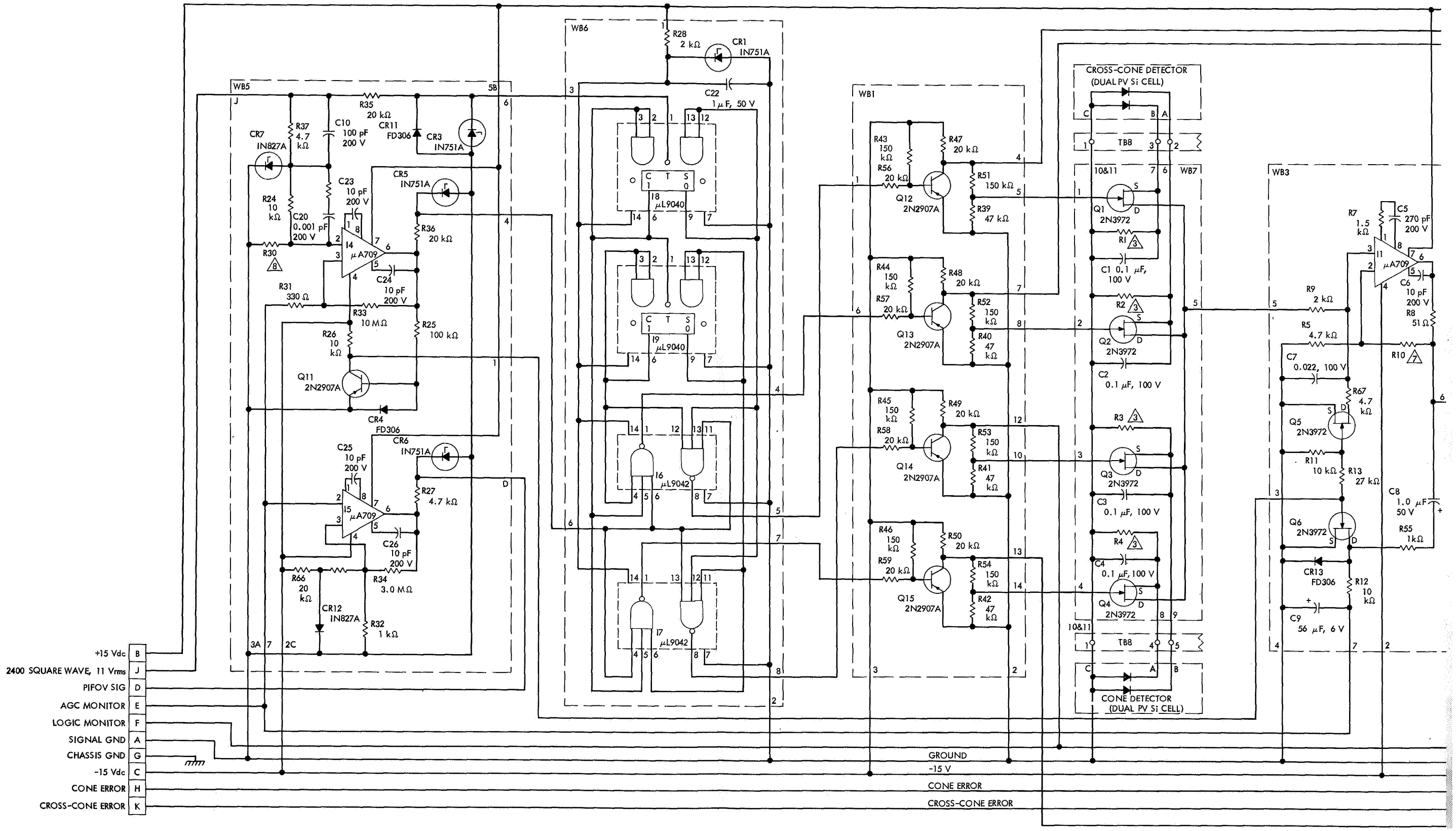
WB5
WB6
WB1
WB7
WB3
CROSS-CONE DETECTOR
(DUAL PV Si CELL)
CONE DETECTOR
(DUAL PV Si CELL)
TB8
R28 2 kΩ
CR1 IN751A
C22 1 μF, 50 V
R35 20 kΩ
CR7 IN827A
R37 4.7 kΩ
C10 100 pF 200 V
CR11 FD306
CR3 IN751A
CR5 IN751A
C23 10 pF 200 V
R24 10 kΩ
C20 0.001 pF 200 V
R36 20 kΩ
R30
μA709
C24 10 pF 200 V
R31 330 Ω
R33 10 MΩ
R25 100 kΩ
R26 10 kΩ
Q11 2N2907A
CR4 FD306
CR6 IN751A
C25 10 pF 200 V
R27 4.7 kΩ
C26 10 pF 200 V
R34 3.0 MΩ
R66 20 kΩ
CR12 IN827A
R32 1 kΩ
18 μL9040
19 μL9040
16 μL9042
17 μL9042
R43 150 kΩ
R56 20 kΩ
R47 20 kΩ
Q12 2N2907A
R51 150 kΩ
R39 47 kΩ
R44 150 kΩ
R57 20 kΩ
R48 20 kΩ
Q13 2N2907A
R52 150 kΩ
R40 47 kΩ
R45 150 kΩ
R58 20 kΩ
R49 20 kΩ
Q14 2N2907A
R53 150 kΩ
R41 47 kΩ
R46 150 kΩ
R59 20 kΩ
R50 20 kΩ
Q15 2N2907A
R54 150 kΩ
R42 47 kΩ
10&11
Q1 2N3972
R1
C1 0.1 μF, 100 V
R2
Q2 2N3972
C2 0.1 μF, 100 V
R3
Q3 2N3972
C3 0.1 μF, 100 V
R4
Q4 2N3972
C4 0.1 μF, 100 V
R7 1.5 kΩ
C5 270 pF 200 V
C6 10 pF 200 V
R8 51 Ω
R9 2 kΩ
R5 4.7 kΩ
R10
C7 0.022, 100 V
R67 4.7 kΩ
Q5 2N3972
R11 10 kΩ
R13 27 kΩ
C8 1.0 μF 50 V
Q6 2N3972
R55 1kΩ
CR13 FD306
R12 10 kΩ
C9 56 μF, 6 V
+15 Vdc B
2400 SQUARE WAVE, 11 Vrms J
PIFOV SIG D
AGC MONITOR E
LOGIC MONITOR F
SIGNAL GND A
CHASSIS GND G
-15 Vdc C
CONE ERROR H
CROSS-CONE ERROR K
GROUND
-15 V
CONE ERROR
CROSS-CONE ERROR

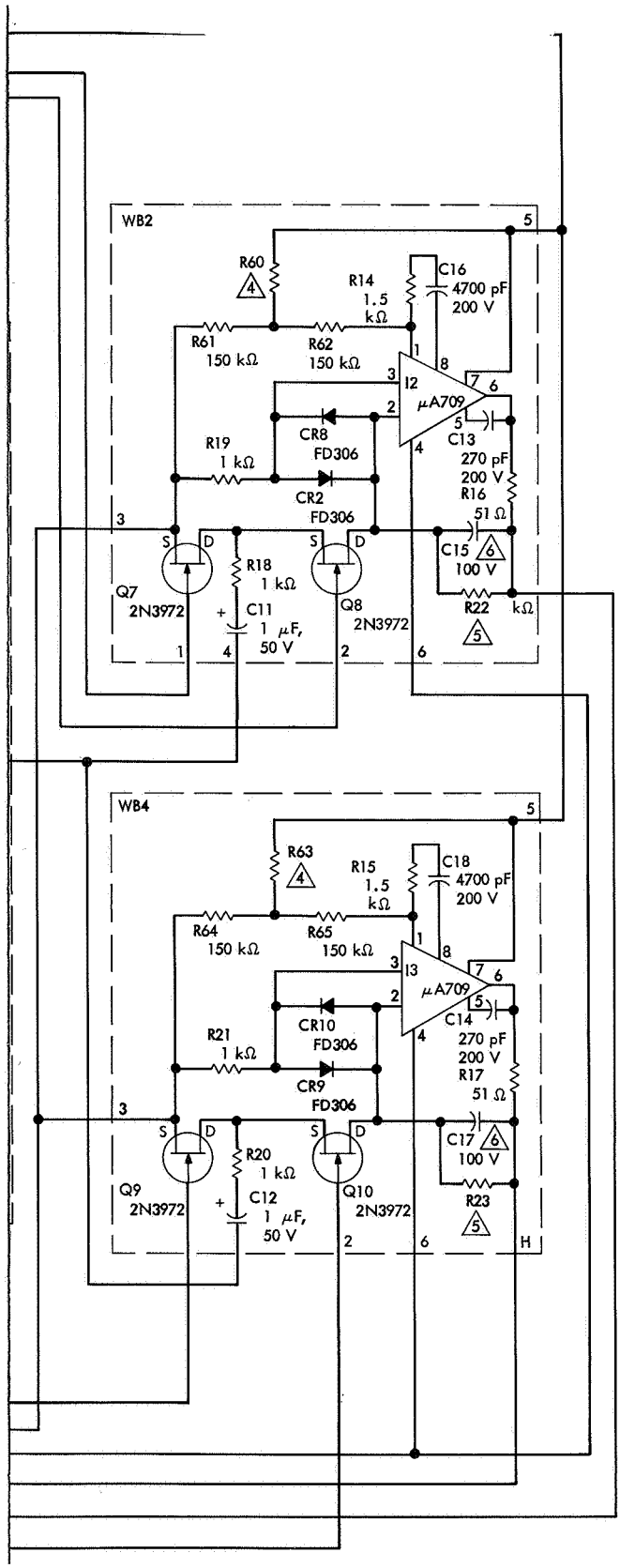

REFERENCES

WIRING BOARD	ASSEMBLY DRAWING
WB1	10018580
WB2	10018582
WB3	10018584-1 10018584-2
WB4	10018586
WB5	10018588
WB6	10018590

REFERENCE DESIGNATIONS

USED	NOT USED
R1 THRU R67 C1 THRU C26 CR1 THRU CR13 Q1 THRU Q15 I1 THRU I9 J1	C10, C21

8 SELECTED TO SET AGC THRESHOLD
7 SELECTED TO SET AMPLIFIER GAIN
6 SELECTED TO SET FREQUENCY RESPONSE
5 SELECTED TO SET AMPLIFIER GAIN
4 SELECTED TO NULL AMPLIFIER
3 SELECTED TO NORMALIZE DETECTOR RESPONSIVITY, R ≃ 47 k

NOTE
UNLESS OTHERWISE SPECIFIED,
(1) ALL RESISTORS ARE 1/4-WATT
(2) ALL CAPACITORS ARE IN MICROFARADS

Fig. 11. Schematic diagram of the FEPS electronics

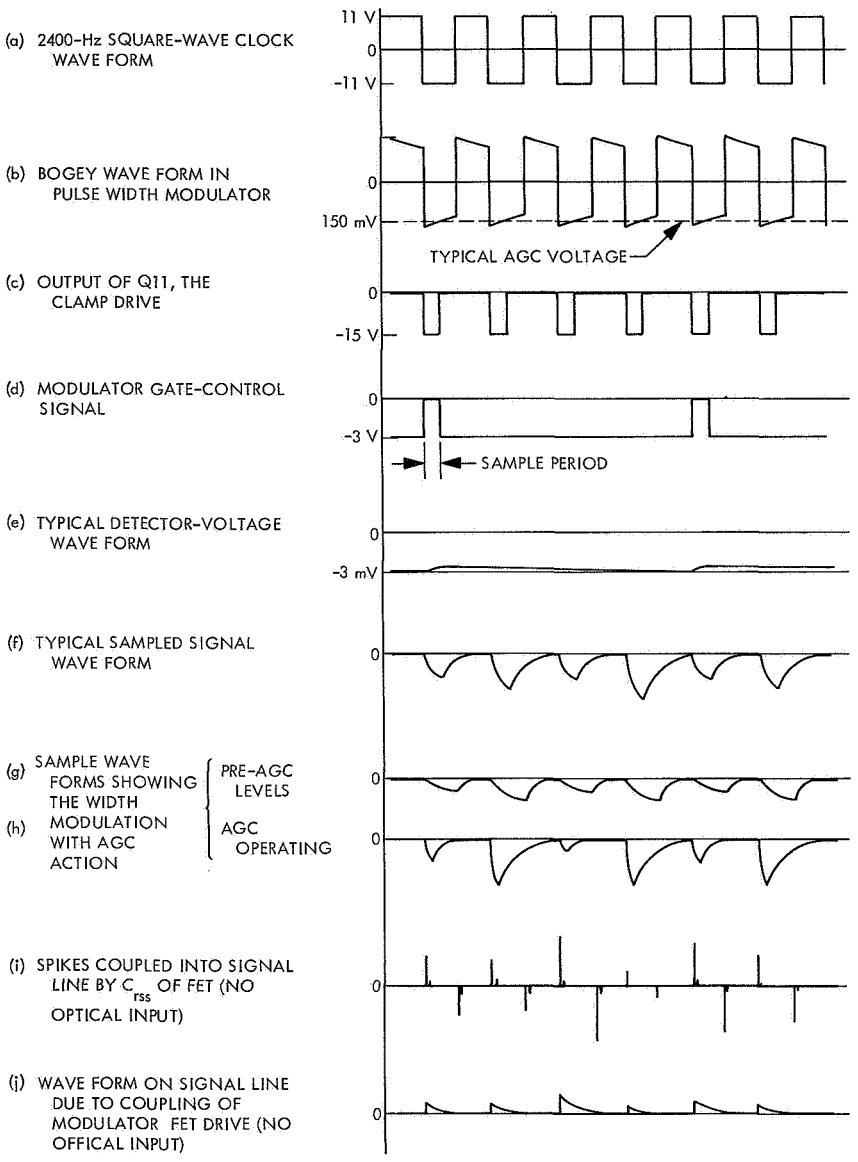

Fig. 12. System wave forms

3. Sampling circuit. The sampling circuit sequentially samples the voltages generated by each of the detector half-cells at a rate of 600 times per second. The sample circuitry, located on WB7, consists of four field-effect transistors (FET), one for each of the detector half-cells. The source-drain circuit of each FET is in series with the signal path from each half-cell to a common junction point. The control signal to the gate of the FET is illustrated in *d* of Fig. 12. The *off* voltage is approximately −3.2 V; the *on*, or sample, voltage is approximately zero volts. The *on* duty cycle varies from a maximum of 12.5% (approximately 0.208 ms) at minimum planet intensity to 1% or 2% at maximum planet intensity. The control logic steps the gating pulse sequentially to each of the four sampling FETs to give a complete frame of tracking information every 1⅔ ms.

The very low signal level in the FEPS and the fairly high impedances make this circuit susceptible to extraneous inputs. One such input that has been noted during testing will be described here because of its influence on the stability of the FEPS.

4. Gate control signal coupling. Every FET has capacitance between the control terminal (gate) and the controlled terminals (source and drain). The FETs used

here (2N3972s) have a specified "small-signal, common source, short circuit reverse transfer capacitance" (C_{rss}) of 6.0 pF maximum. The voltage between the gate and the other terminals is −12 V for this C_{rss} specification. However, the capacitance is not constant with gate voltage but varies in a manner typical of a back-biased diode, causing the capacitance at −3 V to be substantially greater than that at −12 V. From this condition it can be seen that the gate drive signal will be coupled into the signal line. See *i* and *j* of Fig. 12 for the typical signals. The nature and effect of this coupling can be best understood by considering just how the detector signals are processed by the subsequent circuitry.

The sampled signals from the detector are fed into an RC FET-clamp circuit (R9, C7, Q5). The idealized square sample pulse is filtered to the general shape shown in *g* and *h* of Fig. 12. These two illustrations of wave forms show the idealized signal (1) at pre-AGC levels, and (2) with AGC operating. The decrease in sample width was due to AGC action.

The function of this network is to shape the sample pulse in such a way that as the AGC shrinks the sample width the pulse approximates a sawtooth shape. The virtue of this pulse shape is due to the relationship between the area of a triangular pulse and a time base. The area of a triangular pulse of this type will vary as the second power of the pulse period, i.e., $A \simeq (T_{period})^2$. The FEPS demodulators are designed to demodulate as a function of the area of the signal sample. Thus variation of the sample width has a powerful effect on the output of the demodulators and, in turn, on system gain. Because the factor by which the demodulator output is reduced is independent of the individual signal samples, a nearly ideal AGC action results.

In reality, however, we find that the drive-pulse coupling through the FET modulator gives some undesired effects, particularly if the coupling varies between the modulators. A slightly exaggerated case is illustrated in *i* and *j* of Fig. 12 for the situation where detector irradiation is zero. The wave form at pin 5 of WB7 is illustrated in *i* of Fig. 12. This wave form is the output of the modulators before it is shaped by the RC-clamp circuit. Ideally, voltage should not be present on this point because the detector voltage outputs are assumed to be zero. Actually we find spikes here owing to the coupling of the control dV/dt. The spikes, which occur during the unclamped portion of the period, are integrated just like a signal by the RC-clamp circuit. The output of this circuit is illustrated in *j* of Fig. 12 for this spiking situation. The wave form is opposite in polarity from that generated by a set of detector signals. The net effect is a partial but nonuniform cancellation of the detector output signal. An offset is therefore generated that must be cancelled by either electrical or mechanical means.

The FEPS zeroing technique is basically electrical because, for zero illumination, it is desirable to have the error output voltage at zero. This would not be possible if mechanical zeroing were used exclusively. This electrical zeroing is accomplished by supplying a bias to the output amplifiers in each channel, a technique that will be discussed later.

5. Voltage amplifier. The commutated detector signals are next amplified by an operational amplifier that consists of a μA709 integrated amplifier operating at a closed loop gain of approximately 600. The gain is adjusted separately on each FEPS to normalize the acquisition threshold. Resistor R10 and R5 form the feedback network that establishes this gain. Resistor R10 is a selected component and is typically 3.0 MΩ. The gain equation (assuming infinite open loop gain) is

$$Q = \frac{R_{10} + R_5}{R_5} \simeq \frac{R_{10}}{R_5}$$

Two roll-off networks, R7 and C5, and C6, are used to lower the open loop high-frequency gain of this amplifier. These networks are required because of the tendency of the amplifier to oscillate.[4]

A conservative option was used in selecting the networks because maximum frequency response was not required. The closed loop gain of the amplifier as configured here is flat to between 50 and 100 kH. This will handle, at a minimum, the fifth harmonic of the 2.4 kH sample rate, far in excess of the frequency response of the RC pulse-shaping network on the input of the amplifier.

The μA709 amplifier, being basically a transistor amplifier, requires a small but finite bias current to operate. Such current becomes significant in this design as operating temperatures approach the lower type-approval (TA) test limit. The equivalent circuit through which the bias currents must flow is illustrated in Fig. 13. The detector load resistors are shown lumped together in

[4]More data can be found on this design in the manufacturer's specification sheet; and in a Honeywell publication entitled "The Care and Feeding of the μA709 Integrated Linear Amplifier."

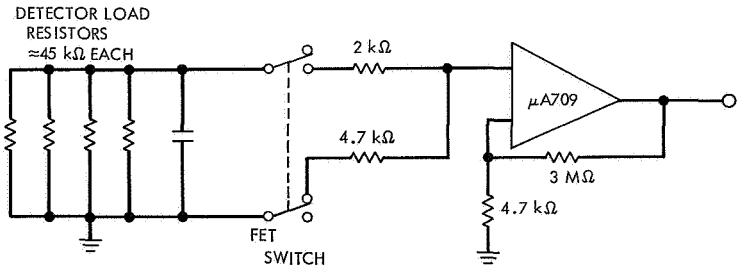

Fig. 13. Equivalent input circuit to voltage amplifier

parallel. They can be simplified in this manner because of the presence of small integrating capacitors that stabilize the voltage drop across each load resistor during the sample frame period. The voltage drop in this circuit is therefore equivalent to that which would be caused by the following unfiltered resistor:

$$R_{eq} \simeq \frac{45\ \text{k}\Omega/4}{2}$$

The factor of two occurs because bias current is drawn from this network only 50% of the time. This percentage is based on pre-AGC conditions. It is at this time that input unbalances have the greatest effect on the tracker error outputs. The equivalent source resistances for each of the two modulation states are then approximately as follows:

Sample

$$R_{eq} \simeq \frac{45\ \text{k}\Omega/4}{2} + R_{FET} + R_9$$

$$\simeq 5.625\ \text{k}\Omega + 50\ \Omega + 2\ \text{k}\Omega \simeq 7.7\ \text{k}\Omega$$

Reset

$$R_{eq} \simeq R_{67} + R_{FET} \simeq 4.7\ \text{k}\Omega$$

At low temperatures, the modulation process will cause a small signal to be developed at the input of the μA709 amplifier. Since the phasing of this signal is the same as a detector-derived signal, a false AGC signal can develop. This effect can be eliminated by making R67 approximately 7.5 kΩ, but this would reduce the effectiveness of the clamp circuit and would, in turn, (1) cause cross-channel interference from the carry-over from one sample to the next, and (2) reduce the efficiency of the AGC demodulator which requires a good zero reference between sample pulses. The value of 4.7 kΩ for R67 represents a satisfactory compromise between these two undesirable effects. To the extent, however, that μA709 amplifiers with smaller bias requirements are obtained or that the lower operating temperature limits are modified, it would be highly desirable to reduce the value of R67. This would increase the effectiveness of the AGC demodulator and extend the range of irradiances over which the FEPS could operate.

6. AGC demodulator. This circuit is a simple synchronous demodulator using a FET clamp to ground between signal samples. During the reference portion of the period a charge is established on C8 through R55 that is analogous to "dc restoration" and is used to eliminate any dc offset from the voltage amplifier. The FET clamp Q6 is next biased *off*, permitting the succeeding signal pulse to couple through R12 and establish a charge on C9. The time constant of this RC network is long, reducing the ripple that would otherwise be imposed on the AGC line by the individual samples. Two components, R55 and CR13, are included in this circuit to prevent overloading at high signal levels. The function of R55 is (1) to minimize the instantaneous current that Q6 must pass to ground, and (2) to prevent a charge from developing on C8 that would drive the drain of Q6 positive during the latter part of the clamp cycle. This possibility arises because the output of the voltage amplifier does not reset to its reference level instantly. The actual wave form during reset has an exponential decay that is caused by the presence of R67 in the input clamp circuit. If the drain of Q6 were driven positive by a significant amount during this part of the cycle, the FET would be "pinched off" and the clamping action would cease. Diode CR13 is connected from the drain to ground to prevent this pinch-off if Q6 should be momentarily overloaded. Thus CR13 delays the overloading of the AGC demodulator that will inevitably occur as planet irradiance is increased beyond normal operating range.

7. Output demodulators. The demodulators develop the tracking error voltage by subtracting the first signal pulse of a detector pair from the second signal pulse. With the designations of the cone axis demodulator referenced, the operation is as follows:

(1) During a cone (cross-cone) sampling period, Q9 (Q7) conducts, causing a charging current to flow through C12 (C11) and R20 (R18). The net charge transferred by this current is proportional to the area of the signal pulse because the RC time constant of this network is long, with respect to the sampling period. This charge develops a voltage across C12 (C11) that is an analog of the irradiance on the corresponding detector sector.

(2) During the subsequent reset period, both Q9 (Q7) and Q10 (Q8) are biased *off*, preserving the charge on the capacitor.

(3) Next, Q10 (Q8) is biased *on* coincident with the sampling of the voltage on the other half of the cone (cross-cone) detector. The charge on C12 (C11) is not significantly altered during this period. The average of this second pulse minus the previous charge on the capacitor is coupled into the input of the integrating output amplifier. This is illustrated in Fig. 14 for three typical tracking situations.

The AGC system, by shrinking the width of these information pulses as the irradiance increases, effectively eliminates the increase in the differential voltage caused by this irradiance increase. The net pulse entering the output amplifier is, thus, an exclusive function of the relative irradiances on the two detector sectors.

8. Output amplifiers. The output amplifiers are basically bandwidth-limited dc amplifiers. The frequency

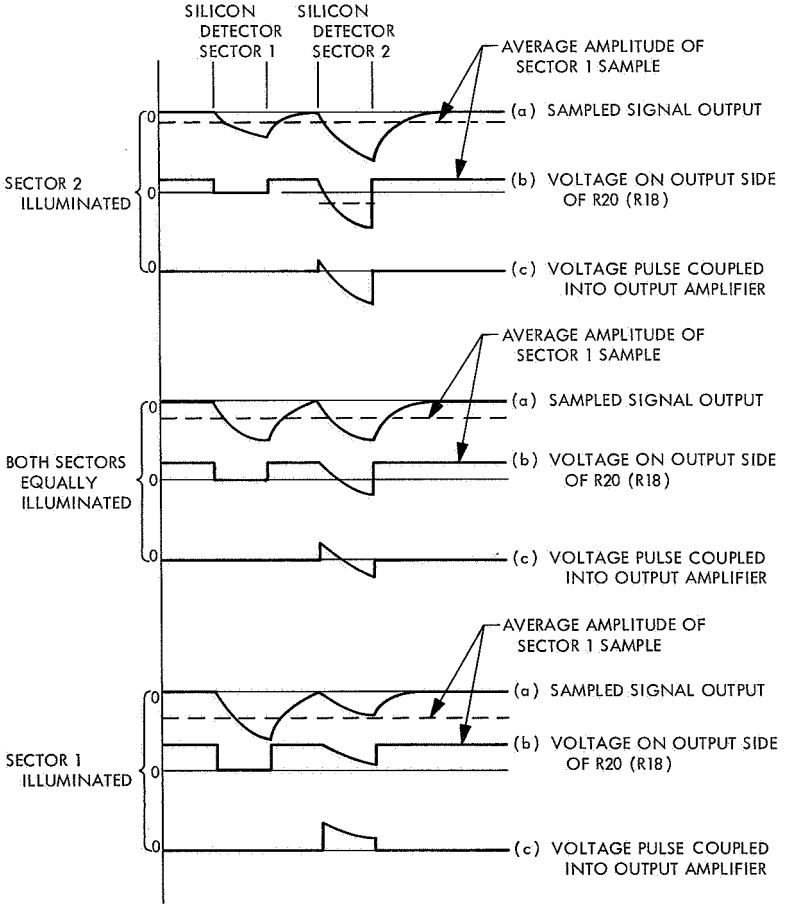

Fig. 14. Typical demodulator wave forms for 3 different tracking error conditions

response is established by the parallel combination of R23 and C17 (R22 and C15). Resistor R23 (R22) establishes the amplifier gain according to the following expression:

$$Q = \frac{R_{23} + R_{20}}{R_{20}} \simeq \frac{R_{23}}{10^3}$$

This gain relationship is, of course, valid only for the period in which Q10 (Q8) is conducting. The gain during the remainder of the time is essentially unity because of the high summing-point impedance when the FET is nonconducting. The frequency response of the amplifier is established by designating a value for C17 (C15) for each possible value of R23 (R22).[5] The net result of these RC combinations is the establishing of the first break frequency for the FEPS output at approximately 14 Hz. A comparison of the amplifier response (14 Hz) with the data rate (600/s) shows that the output amplifiers are effective integrators. The output will then be a dc tracking-error voltage with a small ripple at 600 Hz.

The bias current requirements of the μA709 amplifiers should be discussed here. This bias current, which will be supplied through the feedback network, must be supplied to the input throughout the demodulation cycle, even when the input circuit is open. The net effect will be an output voltage that slowly increases during the period between modulation sampling. This voltage is significant only at temperatures of $-30°$F and lower because of the fall-off in current gain of the input transistors in the μA709 amplifier at low temperatures. The bias current requirements therefore increase to a specified maximum of 1.5 μA at $-55°$C. An analysis of worst-case conditions indicates that the drift in the output voltage at lower-temperature limits will never exceed about 100 mV, an insignificant amount in this system.

The open loop frequency response of this amplifier is limited by two networks: C14 (C13), connected between pins 5 and 6 of the μA709 amplifier; and R15 (R14) and C18 (C16) between pins 1 and 8. These networks were included to prevent possible oscillations caused by phase shift through the integrated amplifier. An extremely conservative set of values for these networks, made possible by the very limited frequency response required from this amplifier, was selected from the manufacturer's tables.

[5]JPL Specification FS503695, "Assembly and Calibration, Far Encounter Planet Sensors (FEPS), *Mariner* Mars 1969 Flight Equipment, Detail Specification."

The resistor R17 (R16), also part of the recommended stabilization network, has the further function of protecting the μA709 amplifier from current surges such as those that might occur during turn-on. If the feedback capacitor did not present a low impedance to these surges, currents could flow that might eventually degrade the output transistors in the integrated amplifier.

A related function is performed by the parallel diodes across the inputs of the μA709 amplifier. These diodes prevent the occurrence of high differential voltages between the two input terminals which might eventually damage the emitter-base junctions of the input transistors. Again, the possibility of such surges of current is due to the capacitive feedback coupling between the output and input circuits.

A trimming circuit consisting of R63, R64, and R65 (R60, R61, R62) is incorporated into each of the output amplifiers to permit the "nulling" of the output voltages. The network provides a small bias current to pin 1 of the μA709 amplifier that can buck system and amplifier offsets to zero. Resistor R63 (R60) is a select component with permissible values ranging from zero to infinity. If we assume a quiescent voltage on pin 1 of +9 V, the bias current can range from -8.2 μA to $+11.8$ μA. *Positive* is defined as current flow into pin 1. The total null range of this circuit on the output at typical gains is approximately 1 V.

Although the trimming circuit was intended by Fairchild[6] to permit the nulling of offsets in amplifier μA709 that inevitably arise from the distribution of internal parameters, its major function is to null offsets that are caused by the modulation process.

9. Pulse width modulator. The pulse width modulator (PWM), located on WB3 along with the PIFOV detection circuit, is the circuit that establishes the duration of each sampling pulse. At pre-AGC irradiance levels the output of the pulse width modulator is essentially a square wave with a period of approximately 416 μs. At irradiance levels above the AGC threshold, the period of the positive portion of this wave shrinks. The detector sampling signals are derived from this wave through the digital logic.

The operation principle of this circuit can be seen from the wave form shown in Fig. 15, in which the pulse width

[6]Located in Mountain View, Calif. 94040.

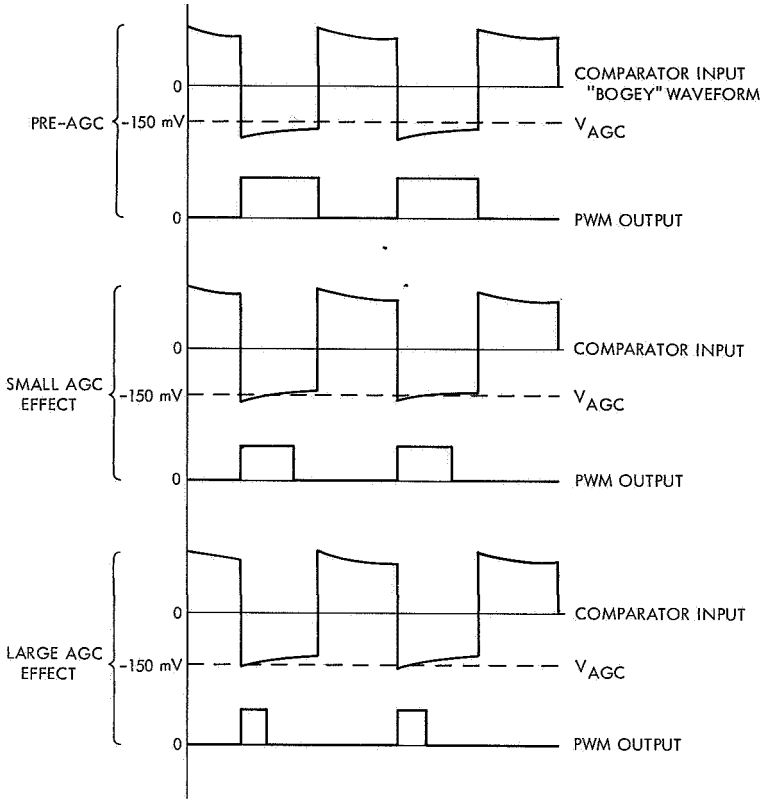

Fig. 15. Pulse width modulator output vs automatic gain control voltage

modulated output is a function of the differential between two voltages. The first voltage is the AGC voltage, which results from the demodulation of all the detector sample pulses. This voltage ranges from approximately zero at no-planet to −165 mV at maximum-planet. The second voltage is a slightly peaked square wave with a zero-to-peak amplitude of approximately 170 mV. This wave is designated the *bogey* wave in the following discussion.

The bogey wave is developed as follows:

(1) A temperature-compensated zener diode CR7 is driven through R37 from the 2400-cycle square-wave line. A square wave of approximately 12 V peak-to-peak is developed across this zener diode. The negative part of the wave, created by controlling the parameters of the zener diode, is of interest here. The positive part of the wave results from the zener breakdown of the normally forward-biased internal diode. This diode provides the temperature compensation for the composite zener assembly. A small peaking capacitor C19 swamps the capacitance of the zener diode, maximizing the output dV/dt.

(2) The "jitter" in the pulse width caused by rippling in the AGC line is held to a constant factor. The simple, tilted, top wave would result in a relative increase in the jitter from pulse to pulse as the AGC voltage increases.

The voltage comparator itself is simply a differential amplifier with a small amount of positive feedback that prevents random "toggling" of the amplifier when both inputs are nearly equal. The feedback is established by R33 and R30, the feedback and summing-point impedances, respectively. The C23 and C24 networks prevent the μA709 amplifier from oscillation due to internal parasitic capacitances. These networks are in line with the manufacturer's recommendations for the μA709 amplifier when it is operated at high gains.

The pulse wave from the voltage comparator is next fed to two different circuits. The first circuit is composed

of Q11 (2N2907A), operating as an inverting driver. The negative-going wave that is developed across R26, the load resistor, drives two FET clamps: the voltage amplifier input clamp and the AGC demodulator clamp. The drive to the voltage amplifier clamp is stepped down by a voltage divider consisting of R13 and R11. The divider, by establishing the drive voltage on the clamp Q5, controls the relative effects of drive-signal coupling into the input of the voltage amplifier. The drive signal is in phase with the modulated detector signals and, if coupled in sufficient amount, would be demodulated and produce a false AGC voltage. An earlier section, in noting that the drive pulse couples through to the modulator FETs, pointed out that this coupling subtracted from the detector signals. The two coupling effects, both undesirable, are then made to cancel each other. The output voltage from the clamp divider was established to accomplish just this effect. The residual AGC will thus be within a few millivolts of zero instead of the 100 mV or so that would result if such a cancellation were not possible.

The second circuit driven by the voltage comparator consists of R26 and CR5 operating as a zener voltage limiter. The output voltage from this network swings from approximately −0.6 V to +5.1 V. This wave form is compatible with the following requirements of the digital logic.

10. Digital logic. The logic circuit in the FEPS is a simple divide-by-four counter followed by four NAND gates. The clock drive to the counter flip-flops I8 and I9 originates with the 2400-Hz square wave, as modified by a limiter and shaper circuit. The circuit consists basically of R35 and CR3 operating as a zener limiter. Diode CR11, connected in parallel with CR3, limits the negative excursion of the square wave. The forward drop across zener CR3 would by itself be sufficient to lock up the flip-flops, particularly at temperature extremes. The flip-flops used here (Fairchild μL9040s) require fast switching of the drive voltage to operate reliably.

The NAND gates I6 and I7 each have three inputs. Two inputs are from the counter flip-flops and the third is from the pulse width modulator. The output from each gate is a variable-width pulse that occurs 600 times a second. Each pulse has a maximum duty cycle of 12.5%, or approximately 208 μs. At maximum AGC, the pulse widths will shrink to approximately 20 to 30 μs. The four outputs from the digital logic are normally positive with a logical *one* represented by a negative-going excursion to approximately zero volts.

The +5.0 Vdc supply voltage required to operate the logic circuits is developed from the +15 Vdc line by a zener regulator composed of R28 and CR1.

11. Gate drivers. The drivers that are required to operate the modulator and demodulator FETs are developed by Q12 through Q16, respectively. These are type 2N2097A *p-n-p* silicon switching transistors operating from the −15 Vdc supply. The input voltage to these transistors are developed through a voltage-shifting network that offsets the gate output voltage about 2 V in the negative direction. The drive transistor is thus *turned on* when the gate output is near zero volts and *biased off* when the output is positive.

The drive output is developed by a set of resistance networks of which R47–R51–R39 is typical. Resistor R47 is the load resistor, while R51 and R39 form a divider to provide the reduced drive required by the modulator FETs. The necessity for reduced drive is due to the coupling problem described previously. The modulator drive voltage swings from zero volts for modulator *on* to approximately −3.2 V for modulator *off*. The demodulator *off* voltage, however, is approximately −13.6 V because of the higher-level signals that must be gated in this portion of the circuit.

12. PIFOV detector. The planet-in-field-of-view detector is basically a voltage level sensor that monitors the AGC voltage. The sensor is a μA709 amplifier operating as a differential amplifier with a small amount of positive feedback. The reference voltage is developed by a temperature-compensated zener regulator followed by a voltage divider.

The zener regulator is composed of R66 and CR12 and operates from the −15 Vdc line. Resistors R29 and R32 form the voltage divider. The output of this divider is approximately −135 mV. Resistor R32 also establishes the summing-point impedance of the feedback network. Resistor R34 is the feedback resistor and provides a hysteresis of approximately 7% between the trigger and the drop-out levels.

The output excursion is tailored to system requirements by a zener limiter consisting of R27 and CR6. The no-planet output is approximately −0.6 Vdc while the PIFOV output is approximately +4.6 Vdc.

IV. Fabrication

Six FEPS units were fabricated for the *Mariner* Mars 1969 program. The first unit was an engineering prototype fabricated at JPL. This unit is close to the configuration of the flight FEPS units, the major deviation being the use of unscreened electronic components. The engineering prototype was fabricated to check out the functional design and operational parameters of the FEPS, since this sensor was a totally new design for *Mariner* Mars 1969.

The next five units were fabricated at the Honeywell Radiation Center (HRC)[7] under contract to JPL. The following is a compilation by serial number and use of the five fabricated units:

S/N 001	Production prototype
S/N 002	Proof test model
S/N 003	Flight spare
S/N 004	Flight model (spacecraft G)
S/N 005	Flight model (spacecraft F)

The production prototype S/N 001 was fabricated using unscreened components to check out the production processes and test procedures of the contractor. The proof test model unit, S/N 002, was to have been fabricated with totally screened electronic components. But because of late delivery schedules of a few components, approximately seven unscreened components had to be used. This has caused no problems, however, in the performance to date. All three flight-model FEPS units used totally screened components. The assembly and calibration procedures to be used in fabricating the FEPS are described elsewhere.[8]

During the fabrication cycle at HRC no major mechanical problems developed that necessitated a change. A number of electronic problems were encountered during the fabrication of the production prototype and proof test model units that required some circuit redesign. During the calibration of the production prototype it was discovered that the AGC and PIFOV threshold could not be brought into specification by the normal calibration procedures. After detailed analysis it was determined that a high internal capacitance of one of the modulating field-effect transistors was causing the problem. It was further determined that this capacitance should be as low as possible and nearly equal in the four modulating FETs. A procedure was then established for selecting groups of these transistors with low matched capacitances to be used in other FEPS units. With the balanced FET capacitances the production prototype calibration was completed successfully.

The proof test model unit was successfully calibrated with the knowledge gained from the previous unit. However, when the unit was subjected to low temperature during type-approval testing the PIFOV circuit gave a PIFOV signal with no applied stimulus. This problem was solved by a redesign of the AGC circuit (component value changes and zener diode addition) that consequently resulted in satisfactory operation in all temperature ranges. When the unit was replaced in the type-approval testing, it again failed – this time when tested under high temperature. The cause of the failure was subsequently determined to be a silicon detector problem. The failure was not due to particular failure of the detector but rather to a difference in temperature coefficients between the two detectors. At the elevated temperature the outputs of the two detectors were separated by a voltage whose magnitude was too great for the processing electronics to handle. When the detector pair was replaced with a pair having matched temperature characteristics, the unit performed satisfactorily. Thus the detector problem was prevented from occurring in the flight units by choosing detector pairs with satisfactory temperature characteristics.

Significant problems were encountered during the screening of the Heliotek[9] silicon detectors. Test results indicated poor detector quality; also very little test repeatability could be accomplished. After HRC and JPL expended considerable effort in analyzing and retesting, they concluded that most of the problems arose from contamination in detector handling and poor test procedures. This conclusion is supported by the fact that once detectors were selected, were installed in a FEPS unit, and were calibrated, no failures or performance anomalies occurred (with the exception of the PTM-unit problem that led to the criteria used in selecting detectors).

[7]Located at 2 Forbes Road, Lexington, Mass. 02173.

[8]JPL Specification FS503695, "Assembly and Calibration, Far Encounter Planet Sensors (FEPS), *Mariner* Mars 1969 Flight Equipment, Detail Specification."

[9]Manufactured by Textron Electronics, Inc., Heliotek Div., Sylmar, Calif. 91342.

V. Test Procedures and Results

A. Functional Tests

All FEPS units have undergone a complete series of functional tests to verify compliance with the design requirements. The following specific functional tests were performed:

(1) Transfer curve characteristics

(2) Orthogonality

(3) Mounting alignment

(4) PIFOV signal characteristics

(5) PIFOV threshold

(6) Resolution

(7) Accuracy

(8) Bandwidth measurement

(9) Voltage and frequency margin

The functional test setup used in all testing of the FEPS is shown in Fig. 16. The FEPS is rotated about its nodal point, through the collimated bundle of simulated Mars energy, by means of the rotary table and control panel. The rotary table, by means of a coupled potentiometer, sends a position signal to the X-Y-Y′ recorder that indicates the angular position of the table. A simultaneous recording of the error output of the FEPS produces a transfer curve of angular displacement vs FEPS output. Figure 17 shows a sample transfer curve of the cone-error signal for the production prototype FEPS, S/N 001. Also shown in Fig. 17 is the allowable transfer-curve criteria. All FEPS output curves should fall within the envelope when operating between the design limits of encounter minus 48 hours (E − 48 h) to encounter minus 12 hours (E − 12 h). From the transfer curves, such performance characteristics as (1) total angular field-of-view, (2) linear range, (3) linearity, (4) scale factor, (5) accuracy, (6) mounting alignment, and (7) channel separation are obtained and analyzed to ensure compliance with the specified requirements.

During thermal–vacuum test, life test, and test operations on the spacecraft, an operational support equipment (OSE) hood is used to stimulate the FEPS. The hood consists of five collimated planet sources with angular diameters of approximately 0.5 deg. The center source can be adjusted in both axes to provide a null reading from the FEPS. The other four sources are positioned +3 and −3 deg from null in both the cone and cross-cone axes. The hood is mounted to the front of the FEPS and the light sources are remotely controlled from the test console.

Of interest at this point is the Mars simulator used in testing the FEPS. The prime simulator uses a 300-W

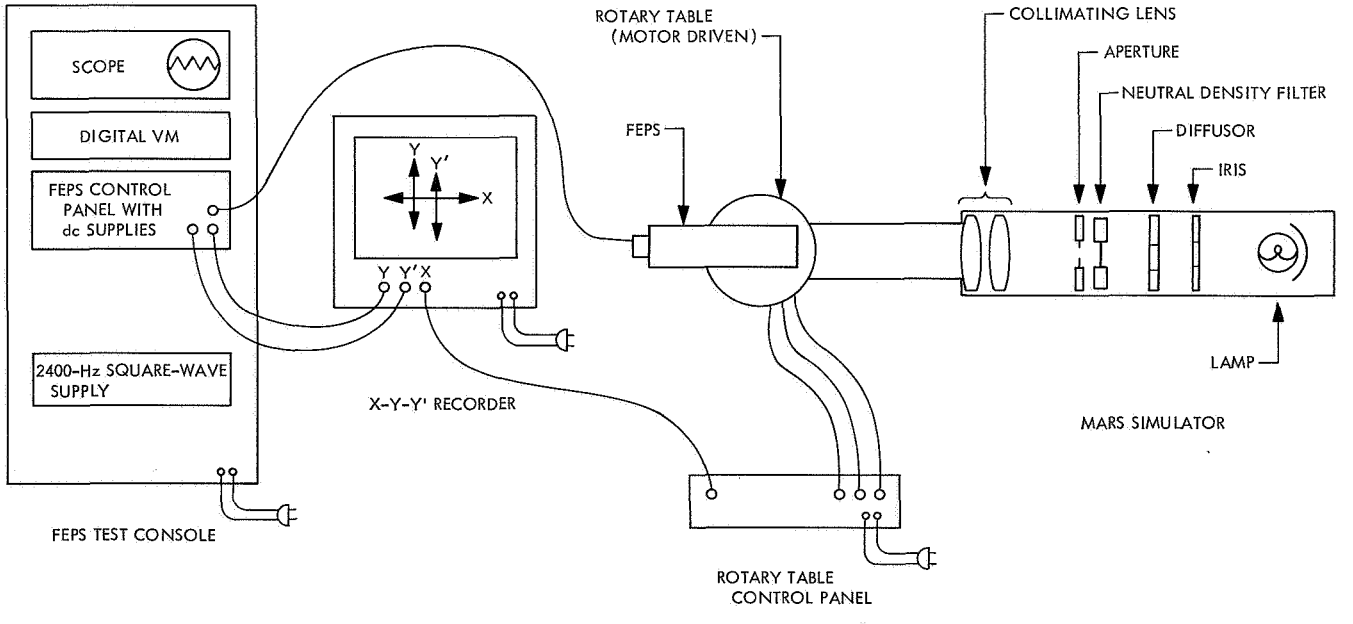

Fig. 16. FEPS functional test facilities

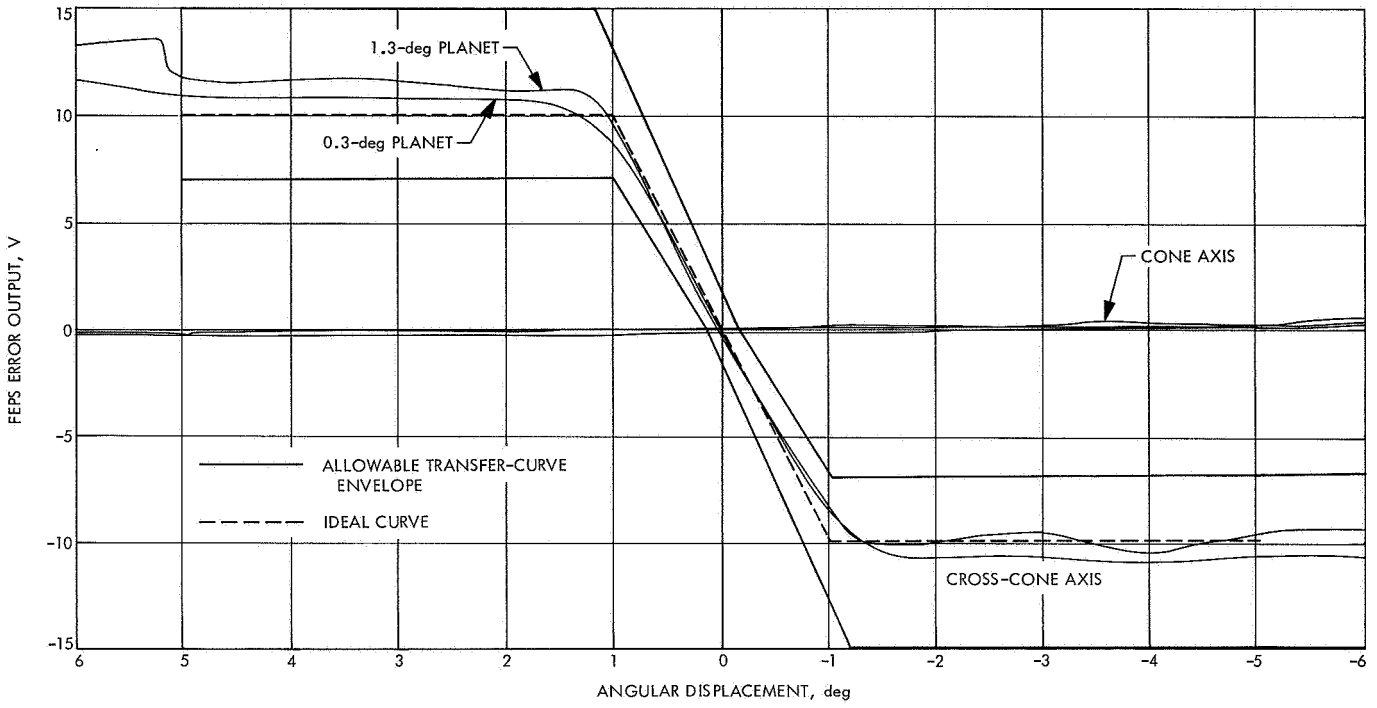

Fig. 17. FEPS transfer-curve criteria with actual curve

tungsten filament projection lamp as a source. This simulator was spectrally calibrated using a Cary 14 spectroradiometer.[10] To account for the spectral difference between Mars, the simulator, the FEPS, and the Pritchard photometer (used to measure source intensity),[11] a mathematically derived correction factor R was determined. The desired Mars intensity (in foot-candles) multiplied by the correction factor R equals the Pritchard photometer reading (in foot-candles).

The prime simulator was used by HRC in the calibration and testing of all the FEPS. The simulator used by JPL for FEPS testing is a different design from that of the prime simulator, but was modified to use the same type of source lamp. It was then calibrated by transferring the calibration from the prime simulator by means of two FEPS units. Since then, both simulators have provided similar test results.

B. Extended-Operation Tests

The original *Mariner* Mars 1969 design requirements of the FEPS require the device to point to the center of

[10]Manufactured by Cary Instruments, Monrovia, Calif. 91016.

[11]Photo Research Corp., 837 N. Cahuenga Blvd., Hollywood, Calif. 90028.

Table 2. Null error at ambient temperature

FEPS unit	Time from encounter, h					
	78	60	48	12	7.5	4.0
S/N 003						
Cone	−0.22	−0.17	−0.14	−0.05	−0.19	—[a]
Cross cone	−0.12	+0.06	+0.01	−0.05	−0.12	
Vector sum	0.25	0.18	0.14	0.07	0.22	
S/N 004						
Cone	−0.14	−0.09	−0.08	0	−0.09	+0.5
Cross cone	+0.12	+0.07	+0.06	+0.02	−0.04	+0.22
Vector sum	0.185	0.115	0.105	0.02	0.10	0.56
S/N 005						
Cone	−0.20	−0.14	−0.10	−0.02	−0.17	−0.75
Cross cone	+0.10	+0.05	+0.02	−0.07	−0.15	−0.5
Vector sum	0.23	0.15	0.10	0.075	0.23	0.9

[a]S/N 003 will not operate at E − 4 h because of its saturated electronics.
Null error is shown in degrees.

illumination of Mars within an accuracy of 0.2 deg (0.14 deg per axis). The nominal dynamic range of operation must extend from $E - 48$ h to $E - 12$ h. A third requirement defines the scale factor of the output transfer function as 10 V/deg ±30%. Functional test data for the flight sensors S/N 003, S/N 004, and S/N 005 show that the requirements are met by all three sensors.

Present far-encounter-sequence planning requires the FEPS to operate over a dynamic range of $E - 76$ h to $E - 4$ h.

The following discussion covers the testing performed at JPL to provide data on the operational performance of the FEPS to these extreme operating requirements.

1. Test conditions. In all tests conducted with the FEPS, a simulator with a uniformly illuminated, collimated disc with the following characteristics was used:

Time from encounter, h	Mars diameter, deg	Mars illumination at sensor, ft-cd
$E - 78$	0.25	0.00175
$E - 60$	0.25	0.0028
$E - 48$	0.3	0.0045
$E - 12$	1.3	0.0725
$E - 7.5$	1.9	0.214
$E - 4$	4.0	0.670

These sizes do not represent the actual diameter of Mars at the corresponding distance, but are sized by the available simulator aperture that comes the closest to the average actual size of the planet over four possible launch dates and trajectories – February 16 and 28, March 8, and April 18. These errors between the actual and the simulated diameters offer only second-order errors to the FEPS data.

Illumination values represent an average of illuminations over the same four launch dates and trajectories. The maximum spread between illumination values at a given distance over the four launch dates is 13%.

2. Null accuracy. Table 2 gives sensor null error (null offset) in degrees with respect to time from encounter. Both the individual axis error and the overall vector sum of the two errors are presented. All measurements are made at room temperature.

These data show that the largest null error is 0.25 deg at $E - 78$ h from S/N 003.[12] The allowable error is 0.20 deg.

From the functional tests performed on the three flight units and the proof-test-model unit, the stability, or repeatability (at room temperature), of the null error is determined as being in the order of ±0.01 deg or better.

The effect of temperature on the null pointing is small. The values given in Table 3 represent null shift that is due to temperature at −4°F. These values are presented in the form of correction factors for Table 2. To determine the null error at −4°F algebraically, add the values in Table 3 to the corresponding values in Table 2. A linear extrapolation of the correction factors will give a good approximation of null errors at any temperature between 75°F and −4°F.

Table 3. Null error correction factors for −4°F

FEPS unit	Cone	Cross cone
S/N 003	+0.01	−0.03
S/N 004	−0.015	+0.055
S/N 005	−0.03	−0.01

3. Scale factor. Table 4 gives the transfer function scale factors for the three flight sensors from $E - 78$ h to $E - 4.0$ h.

4. Planet-in-field-of-view signal. The nominal requirement for the FEPS to produce the PIFOV signal is that the signal appear at $E - 48$ h or earlier. Table 5 gives the actual time from encounter that the signal will actuate for each of the three units.

5. Extended-operation test conclusions. The results of JPL tests show that the three flight-model planet sensors will operate satisfactorily from $E - 78$ h to $E - 7.5$ h. The desired null pointing accuracy of 0.2 deg is met only by S/N 004. Both S/N 003 and S/N 005 have somewhat larger errors at these extended operating ranges, although

[12]Sensor S/N 003 will not operate at $E-4$ h because of electronics saturation caused by high illumination from planet.

Table 4. FEPS transfer function scale factors

FEPS unit	Time from encounter, h					
	78	60	48	12	7.5	4.0
S/N 003						
Cone	6.6	8.7	10.5	12.0	3.5	—[a]
Cross cone	3.8	8.7	10.5	11.8	3.8	
S/N 004						
Cone	4.4	6.7	9.5	14.3	6.0	1.5
Cross cone	3.5	5.7	8.0	12.3	12.5	2.1
S/N 005						
Cone	5.6	8.7	9.4	11.4	3.8	0.2
Cross cone	5.4	7.5	9.0	11.4	5.5	1.0

[a]S/N 003 will not operate at $E - 4$ h because of its saturated electronics.
Scale factor values are given in volts per degree.

Table 5. PIFOV actuation time

FEPS unit	Time from encounter, h
S/N 003	$E - 69 \pm 5$ h
S/N 004	$E - 57 \pm 5$ h
S/N 005	$E - 65 \pm 5$ h

the largest error seen is 0.25 deg. The scale factors decrease at far and near extremes because of lack of dynamic range of the internal AGC system of the planet sensor, but this decrease will have only second-order effects on null pointing accuracy.

For operation between $E - 7$ h and $E - 4$ h the FEPS will exhibit null errors greater than 0.2 deg, as shown in Table 2, and highly degraded scale factors, as shown in Table 4. The planet sensor S/N 003, because of electronic saturation, will not operate closer than $E - 7$ h. The planet sensor S/N 004 will be used on Mission G, which is designed to operate, in the far encounter mode, to $E - 4$ h 26 min. The planet sensor S/N 005 will be used on Mission F, scheduled for operation to $E - 7$ h.

C. Environmental Tests

The proof-test-model planet sensor S/N 002 was subjected to type-approval testing both at Honeywell and at JPL. The sinusoidal and random vibration tests and thermal–vacuum tests were conducted by HRC. Thermal–vacuum testing was accomplished in the HRC facility and vibration at the Acton Test Laboratories.[13] Testing at JPL included static acceleration and humidity tests. The engineering prototype fabricated at JPL had previously been successfully tested to type-approval levels of pyro shock and acoustic shock.

The only failures in the type-approval environmental test were those that occurred during thermal–vacuum testing at HRC (see Section IV). No mechanical failures of any sort occurred during any type-approval test.

The three flight-model planet sensors were subject to flight-acceptance levels of thermal–vacuum tests and sinusoidal and random vibration tests, with no failures or anomalies.

D. Life Test

The proof-test-model planet sensor S/N 002 was installed in a life test configuration on October 18, 1968. The unit is being operated at ambient temperature and pressure for a period of nine months, during which time it has remained in a *power on* condition with no optical input. At specified monthly periods the unit has undergone a series of margin tests using an operational support test hood as the optical stimulus.

Testing to date has shown no operational degradation or anomalies. It is planned to conclude this test by running it the last three days with an optical input to simulate the encounter condition.

VI. Conclusions

The design, fabrication, and test of the FEPS has proceeded from January 1967 to August 1968. All the original design requirements have been met or exceeded. Detailed tests were conducted on each flight-model planet sensor to establish individual operating characteristics for revising the encounter sequence by enlarging the required dynamic range of FEPS operation. These tests show that satisfactory operation of the FEPS is anticipated as close as $E - 4$ h 25 min, rather than at the original design requirement of $E - 12$ h.

[13]Located in Acton, Mass. 01720.

Appendix A

Calculation of the Center of Brightness of Mars

I. Introduction

The *Mariner* Mars 1969 scan platform will be directed toward Mars in the far encounter mode by the far encounter planet sensor. The FEPS will point to the center of brightness of Mars, which is not necessarily the geometric planet center. A study that was undertaken to determine the planet's center of brightness with respect to its geometric center gave the following results.

Six calculations were made to determine the center of brightness for five different rotational positions of Mars with respect to the spacecraft. Table A-1 is a list of the cases explored. From these six cases, the center of brightness was found to fall within a circle whose diameter is only one-twelfth the planet diameter and whose center is located midway between the geometric center and the subsolar point of the planet. The spread of calculated brightness centers is shown in Fig. A-1. The six cases are shown in Figs. A-2 through A-6.

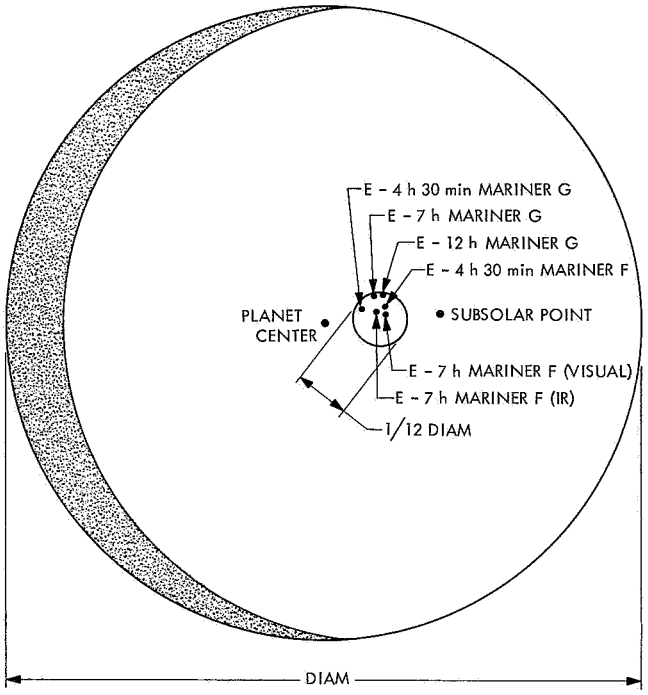

Fig. A-1. Center of brightness dispersion for Mars

II. Discussion

The simplified method of calculating the center of brightness of Mars has given consistent results despite the large differences of surface features. The basis for the calculations was a *Roth globe*, which is a model of Mars. This model is hand-painted by James Roth, who is under contract to JPL. Mr. Roth does the research necessary to provide the proper surface-feature contrasts for the particular seasons in question. The model was photographed as Mars would be seen from the spacecraft at the times given in Table A-1, using a source of illumination (simulating the sun) located at a phase angle of 23 deg.

Each of the surface features on the photographs was then lined off with respect to equal-brightness ratios. The ratios used in this study are shown in Table A-2.

The infrared values were used, since both Mars and the FEPS have spectral characteristics peaking in the near infrared. Case 5 was calculated using both the infrared and visual ratios, and no significant differences were obtained between the infrared and visual centers of brightness.

After the photos were filled in with the proper brightness ratio, a grid overlay containing 144 squares was laid

Table A-1. List of cases

Case	Spacecraft	Time	Spectrum	Figure
1	*Mariner G*	*E* − 4 h 30 min	Infrared	A-2
2	*Mariner G*	*E* − 7 h	Infrared	A-3
3	*Mariner G*	*E* − 12 h	Infrared	A-4
4	*Mariner F*	*E* − 4 h 30 min	Infrared	A-5
5	*Mariner F*	*E* − 7	Visual	A-6
6	*Mariner F*	*E* − 7	Infrared	A-6

Table A-2. Brightness ratios for surface features of Mars

Surface feature	Brightness (Visual)	Brightness (Infrared)
Dark mare	0.5	0.3
Bright desert	1.0	1.0
Elysium, Hellas	1.1	1.0
Sinus	0.7–0.8	0.55–0.7
"Dark" desert	0.9	0.85
Polar cap	1.2	1.0

on the photo and each square assigned a number corresponding to the visually estimated brightness ratio within that square.

It was then necessary to multiply each brightness ratio by an appropriate cosine function to account for reflection from a spherical body. This was accomplished by superimposing an overlay upon the grid. This second overlay consisted of a set of ellipses representing circles that emanated from the subsolar point on the planet. Each ellipse corresponded to a certain angular distance from the subsolar point.

Each brightness ratio of the underlying grid was then multiplied by the appropriate cosine of the angle depicted on the second overlay. The results of each operation were tabulated on another grid that was then numerically integrated to determine the mathematical center which corresponded directly to the center of brightness.

This entire procedure was followed for each of the six cases. As Fig. A-1 shows, the results are surprisingly consistent. At $E-12$ h the center of brightness is approximately 0.14 deg from the geometric center of the planet. At $E-7$ h it is approximately 0.17 deg, and at $E-4$ h 30 min it is approximately 0.4 deg.

No calculation was made for the case of Mission F spacecraft at $E-12$ h, since the photo showed surface features similar to the spacecraft G case at the same distance. Note that the infrared brightness ratios used in Table A-2 are not derived from empirical data, but are engineering estimates based on the accepted visual ratios.

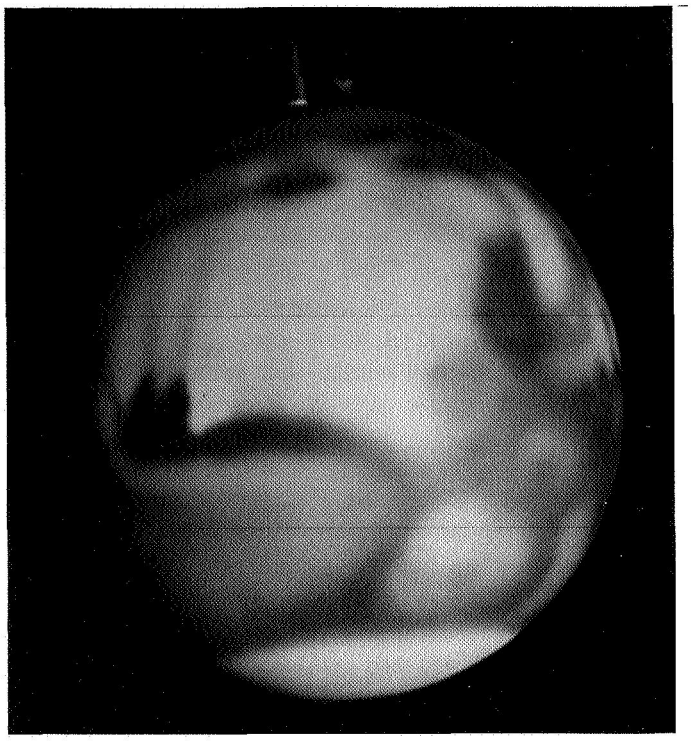

Fig. A-2. *Mariner* G at *E* − 4 h 30 min

III. Conclusion

This study has shown that the contribution of surface features to a shift in the center of brightness of Mars is small and, indeed, could well be neglected. One would not be far wrong if he took the center of brightness to be midway between the geometric center and the subsolar point, as it would be with a perfectly uniform planet.

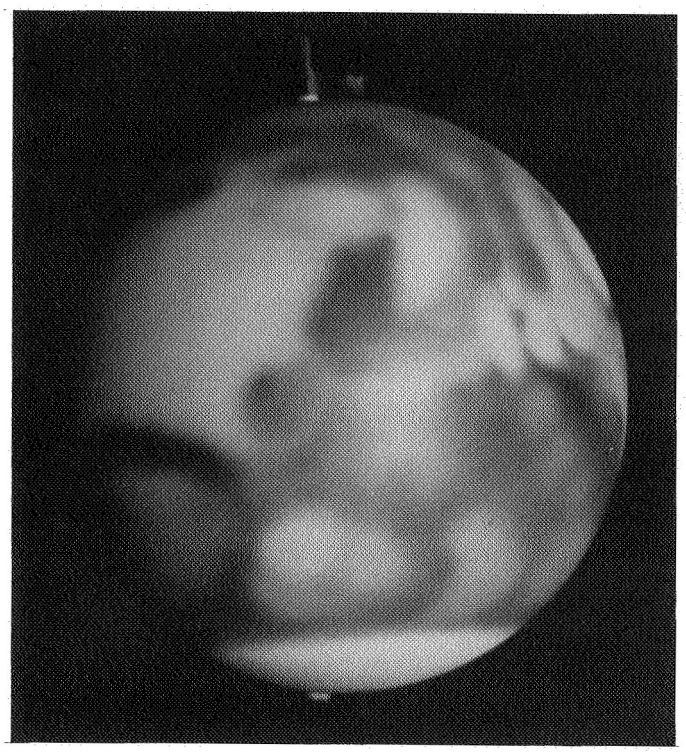

Fig. A-3. *Mariner G* at *E* − 7 h

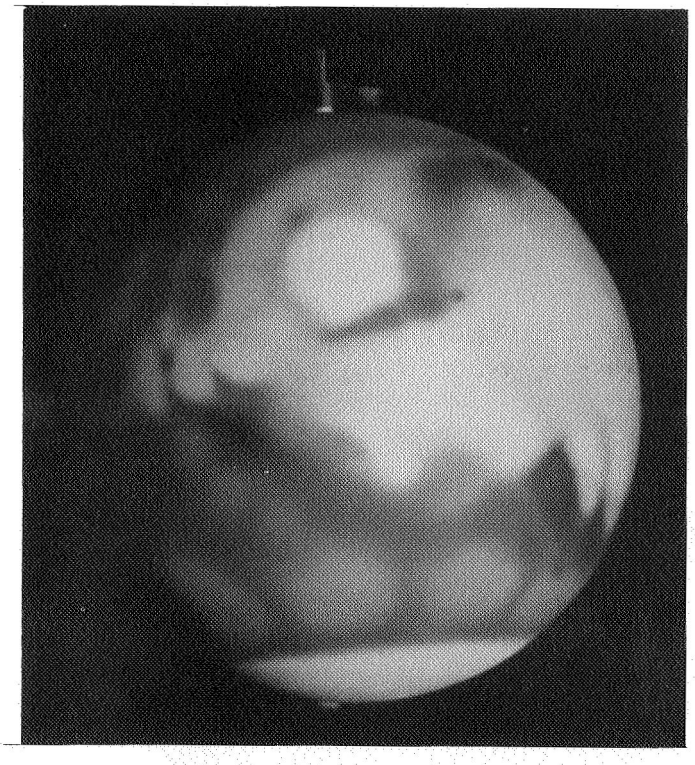

Fig. A-4. *Mariner G* at *E* − 12 h

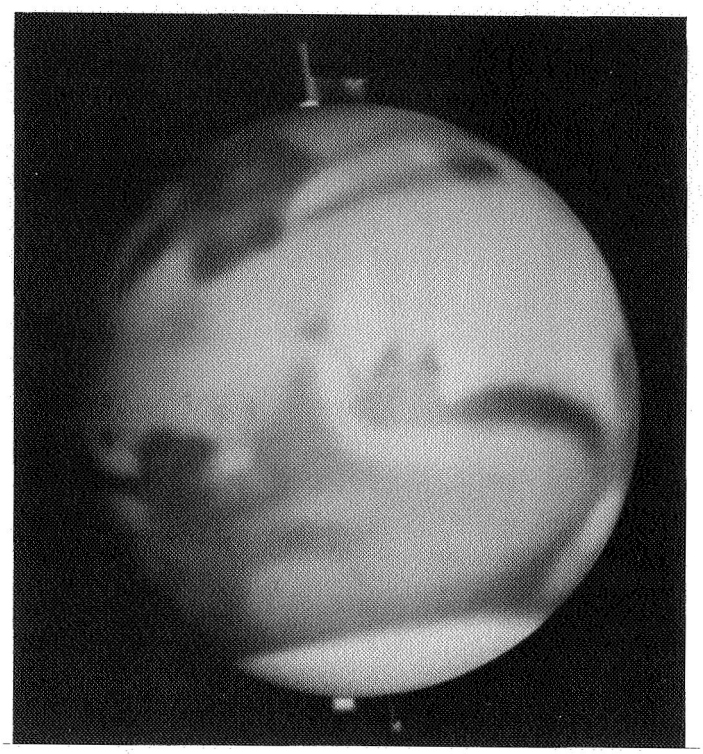

Fig. A-5. *Mariner F* at *E* − 4 h 30 min

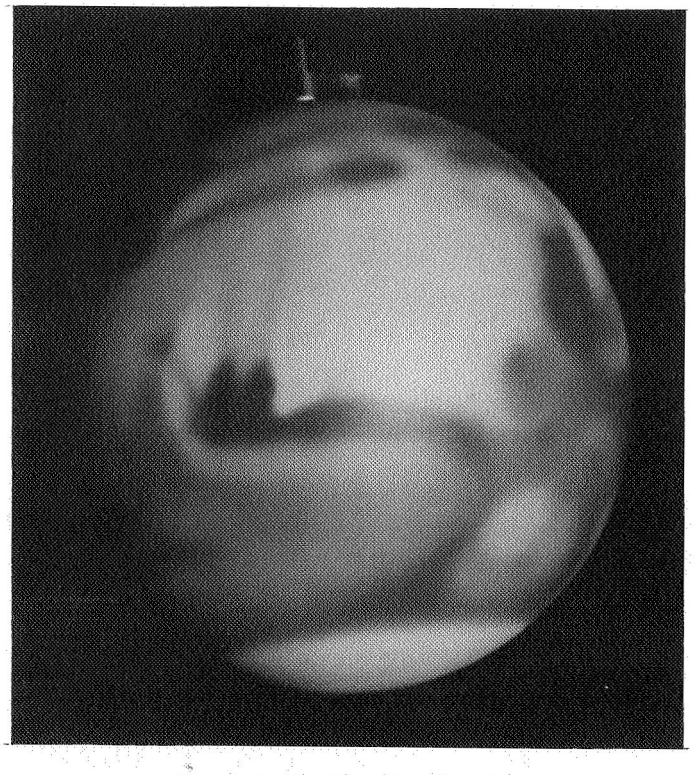

Fig. A-6. *Mariner F* at *E* − 7 h

Appendix B

Specification for Silicon Detectors

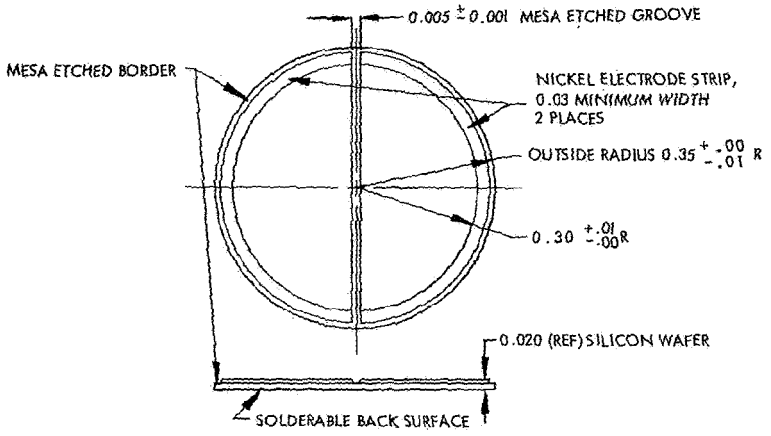

FIGURE 1

NOTES:

1. Part Number *Example* ..... ST 10634-1
2. *Unless otherwise specified, dimensions are in inches and shall* be interpreted per MIL-STD-8C; Tolerance as shown in *FIGURE 1.*
3. Materials:
   a. *Cell:* N on P silicon, 10 ohm-cm, diffused for 90 minutes (minimum).
   b. *Electrodes:* Electroless nickel; thickness adequate to permit soldering of leads to electrode surface.
4. Finish:
   Active areas of each half of the dual cell shall have a silicon monoxide anti-reflection coating.
5. Construction:
   a. Prepare from a single crystal flake by Mesa etch technique to define active cell areas.
   b. Following the Mesa etch process, the cell material shall be maintained in a moisture-free environment by individually bagging cell or by storage in a moisture-free area.
6. Assembly:
   Attach leads to electrodes by soldering, using low-melting point solder after pre-heating detector on a hot plate.
7. Electrical characteristics:
   (The following tests shall be performed with the cell un-illuminated)
   a. Polarity: Back surface is anode common to both active cell areas.
   b. Reverse current: At 0.5 VDC back bias, the leakage of each half-cell shall be less than one microampere.
8. *This Standard* takes precedence over documents referenced herein.

APPROVED: A 5 6 REVISED: (B)

APPROVED SOURCE(S)			ONLY THE ITEM(S) LISTED IN THE APPROVED SOURCE BLOCK AND IDENTIFIED BY VENDOR(S) NAME(S), ADDRESS(ES), AND PART NUMBER(S) HAS BEEN TESTED AND APPROVED BY THE JET PROPULSION LABORATORY OR ITS DELEGATED ALTERNATE. A SUBSTITUTE ITEM SHALL NOT BE USED WITHOUT PRIOR TESTING AND APPROVAL BY JPL OR ITS DELEGATED ALTERNATE.
VENDOR PART NO.	VENDOR	JPL PART NO.	
NONE	HELIOTEK, DIV. OF TEXTRON ELECTRONICS, INC. 12500 GLADSTONE AVE. SYLMAR, CALIFORNIA (FSCM 09722)	ST 10634-1	

JET PROPULSION LABORATORY CALIFORNIA INSTITUTE OF TECHNOLOGY

Procurement Specification: NONE	TITLE: CELL, PHOTOVOLTAIC, DUAL, SILICON	STANDARD PART ST 10634
Custodian: Standards Group Design Section 356		SHEET 1 OF 2

JPL 0971-4 DEC '66

UNCLASSIFIED

REQUIREMENTS:

I. MANUFACTURING REQUIREMENTS

A. Each unit shall meet the requirements of FIGURE 1 and NOTES.

B. The Manufacturer shall certify, in writing, that each unit has been tested, inspected and qualified (per I. MANUFACTURING REQUIREMENTS, A.).

II. TRACEABILITY

See III. INSPECTION REQUIREMENTS, and V. IDENTIFICATION, C.

III. INSPECTION-REQUIREMENTS

Inspection shall be performed in accordance with the requirements of FIGURE 1 and NOTES. An inspection card printed on sulfur-free stock shall contain (but not be limited to) the information specified in V. IDENTIFICATION, and a record of inspections performed.

IV. SCREENING

Each unit shall be screened by JPL or its delegate to the provisions of JPL Specification ZPP-2073-3016A.

V. IDENTIFICATION

A. Part Number: JPL Part Number (See Note 1) and Vendors Part Number shall be contained on the inspection tag.

B. Date of Manufacture: Date of manufacture and serial number of each unit shall be combined and marked on the inspection card as shown:

(702-397 is used as an example. The numerals shall reflect calendar and manufacturing progression.)

VI. PREPARATION FOR DELIVERY

A. Packaging: Units shall be packaged in individual dual plastic bags. The inner bag shall be of the heat seal type and shall contain a dessicating agent of the silica-gel or equivalent type adequate to maintain a moisture-free atmosphere within the bag. The inner bag together with the inspection card shall be placed in an outer sealable plastic zipper bag.

B. Shipping Container: Commercial shipping container sufficient to prevent damage when shipped by common carrier. Each exterior shipping container shall be durably and legibly marked with adequate instructions to insure that damage during handling and shipping is prevented.

JET PROPULSION LABORATORY CALIFORNIA INSTITUTE OF TECHNOLOGY				
ST 10634	REV B	TITLE: CELL, PHOTOVOLTIAC, DUAL, SILICON		REV
SHEET 2				SHEET

JPL 0971-3 APR 65

UNCLASSIFIED